Photovoltaic (PV) systems produce a significant amount of the electrical energy used around the world. PV technology will be capable of offering a great deal of support in the future to the rate of growth of advanced economies as well as developing countries. The incentives provided at a first stage by the European governments have resulted in the rapid growth of the PV market and an increase in the number and quality of products offered by industry. PV modules by many producers are now commercially available, and a number of power electronic systems have been put on the market for processing the electric power produced by PV systems, especially for grid-connected applications.

1

PV Modeling

1.1 From the Photovoltaic Cell to the Field

Photovoltaic (PV) generators are made of a number of PV cells connected in series and in parallel. The type of connection depends on the voltage and current levels at which it is desired that the power processing system dedicated to the PV generator works. The right choice of the values of such electrical variables is of fundamental importance in determining the efficiency of the switching converters that condition the power produced by the PV generator in order to feed the AC mains or recharge a battery. Unfortunately, in usual applications the voltage and current levels of the PV generator cannot be referred to a single PV cell. In fact, cells are arranged into PV panels, which contain some tens of them connected in series. The choice of connecting the cells in series comes from the fact that their operating voltage is few hundreds of millivolts, while the current they generate at high irradiation levels is of some amperes. As a consequence, the cells series connection leads to PV panels working at few tens of volts and some amperes.

In PV power plants, panels are connected in series to form strings in order to reach a voltage level that meets the input requirements of the power processing system. The desired power level of the PV plant is reached by connecting a number of strings, each one composed of the same number of panels, in parallel, thus leading to an increase of the current level of the PV field.

The nominal current vs. voltage (I-V) characteristic of the whole PV field is obtained by stretching that of the single cell, namely by multiplying the voltage values by the number of cells in series into each panel and then by the number of panels of each string, and by multiplying the cell current values by the number of strings of panels connected in parallel.

Such a voltage and current scaling up holds only under the hypotheses that all the cells are exactly equal and that they work in exactly the same operating conditions, especially in terms of irradiance and temperature. Unfortunately such conditions do not occur in practice because of manufacturing tolerances and aging, so that physical parameters of the cells are different, and because of shadowing, of the different orientation of the cells with respect to the sun rays, due to leaves, bird droppings, and so on.
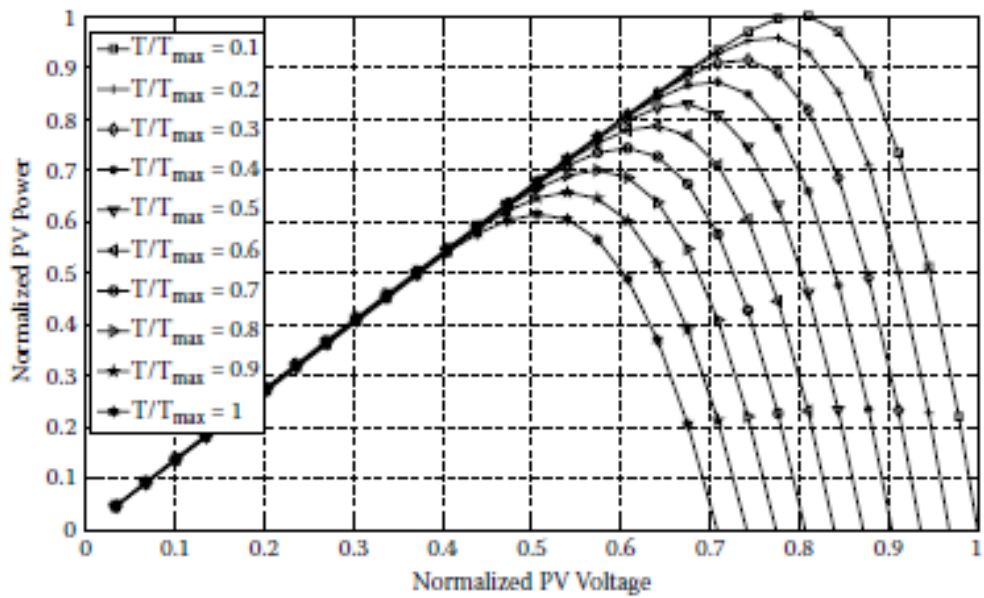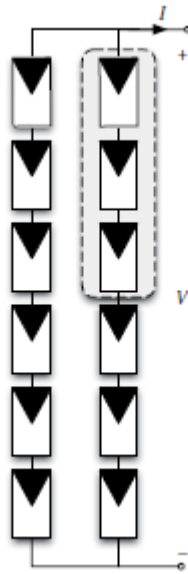
FIGURE 1.5
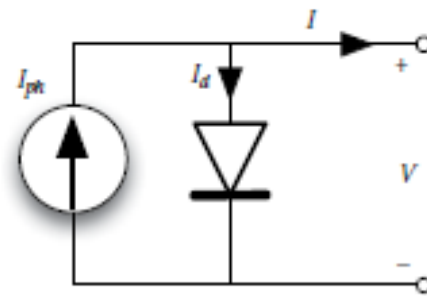Power vs. voltage characteristic of a PV panel: effect of temperature *T*.

FIGURE 1.7
Ideal equivalent circuit of a PV generator.

1.3 The Double-Diode and Single-Diode Models

Looking at the figures shown in the previous section reveals that the I-V curve of a PV generator is obtained by subtracting a diode current, which is nonlinearly dependent on its voltage, from a constant current value. As a consequence, the ideal equivalent circuit shown in Figure 1.7 is made of a current generator in parallel with a diode.

The diode takes into account the physical effects taking place at the silicon p-n junction of the cell. The current generator represents the photo-induced current, which is dependent on the characteristics of the semiconductor material used for the cell, and especially, it is linearly dependent on the cell area, irradiation level, and temperature. Equation (1.2) gives the dependency on the two latter exogenous variables:

$$I_{ph} = I_{ph,STC} \cdot \frac{G}{G_{STC}} [1 + \alpha_I \cdot (T - T_{STC})]$$
(1.2)

where α_I is the temperature coefficient of the current, defined in STC as follows:

$$\alpha_I = \frac{dI}{dT}\Big|_{STC}$$
(1.3)

As a consequence, the I-V characteristic takes the form shown in (1.4).

$$I = I_{ph} - I_{sat} \cdot \left(e^{\frac{V}{\eta V_t}} - 1 \right)$$
(1.4)

where, as usual, V_t is the thermal voltage (1.5):
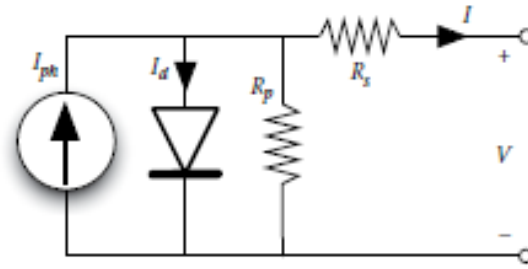
$$V_t = \frac{k \cdot T}{q}$$
(1.5)

FIGURE 1.8
Single-diode model accounting for ohmic losses.

$k = 1.3806503 \cdot 10^{-23}$ J/K is the Boltzmann constant, $q = 1.60217646 \cdot 10^{-19}$ C is the electron charge, and η is the ideality factor. The saturation current is expressed as follows:

$$I_{sat} = C \cdot T^3 \cdot e^{\left(-\frac{E_{gap}}{kT}\right)} \tag{1.6}$$

where E_{gap} is the band gap of the semiconductor material* and C is the temperature coefficient [2].

Such a model does not take into account either the loss mechanisms taking place in the cell due to the metallic ribbon ensuring the current continuity between each cell and the two cells before and after it in the sequence or the diffusion and recombination characteristics of the charge carriers in the semiconductor. Such losses are introduced in the model by adding a series R_s and a parallel R_p resistance in order to take into account internal cell resistances and contact resistances, as well as the effect of leakage currents, respectively. As a consequence, the model becomes the one shown in Figure 1.8.

The series resistance R_s mainly affects the slope of the I-V curves in Figures 1.3 and 1.4 at high voltage levels, namely, approaching the open-circuit voltage: the worse the cell quality, the lower the curve slope, because of a high voltage drop across the series resistance. As a consequence, the approximated definition (1.7) can be adopted:

$$R_s \approx -\frac{dV}{dI}\bigg|_{V=V_{OC}} \tag{1.7}$$

On the other hand, R_p affects the curve slope at current levels close to the short-circuit one: the lower the R_p value, the higher the current drawn by the parallel resistance, which is subtracted from the net output
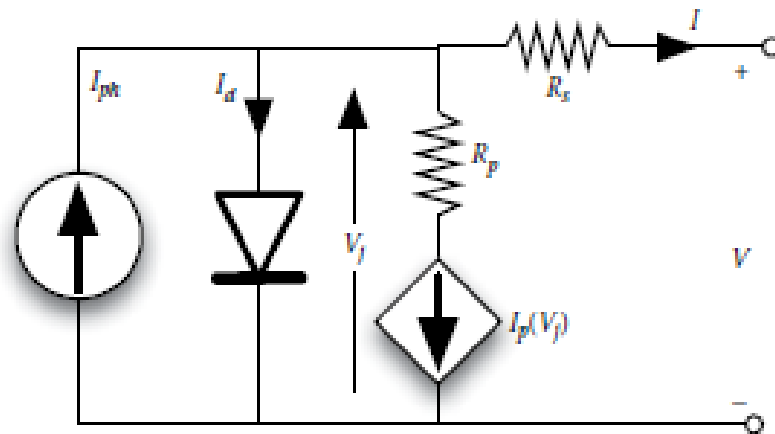
FIGURE 1.10
Bishop equivalent circuit for a counterpolarized solar cell.

$$I_p = \frac{V_j}{R_p}\left[1 + \alpha\left(1 - \frac{V + I \cdot R_s}{V_{br}}\right)^{-m}\right]$$

- Operation in open-circuit conditions: $V_{OC,STC}$
- Open-circuit voltage/temperature coefficient: $\alpha_v = \frac{dV_{OC}}{dT}\Big|_{STC}$
- Operation in short-circuit conditions: $I_{SC,STC}$
- Short-circuit current/temperature coefficient: $\alpha_i = \frac{dI_{SC}}{dT}\Big|_{STC}$
- Operation at the maximum power point: $I_{MPP,STC}$ and $V_{MPP,STC}$

The availability of the set of the parameters listed above allows determining the values of five unknowns. If the single-diode model (1.10) is adopted, the values taken from the data sheet find their counterparts in the unknowns $\{I_{ph}, I_{sat}, \eta, R_s, R_p\}$.

thus the series resistance can be calculated by means of (1.33).

$$R_s = \frac{n_s \cdot \eta \cdot V_{t,STC} \cdot \ln\left(1 - \frac{I_{MPP,STC}}{I_{ph,STC}}\right) + V_{OC,STC} - V_{MPP,STC}}{I_{MPP,STC}} \qquad (1.33)$$

$$I_{MPP,STC} = I_{SC,STC} - \frac{V_{MPP,STC} + R_s \cdot \left(I_{MPP,STC} - I_{SC,STC}\right)}{R_p} +$$

$$- \left(I_{SC,STC} - \frac{V_{OC,STC} - R_s \cdot I_{SC,STC}}{R_p}\right) e^{\frac{V_{MPP,STC} + R_s \cdot I_{MPP,STC} - V_{OC,STC}}{\eta V_{t,STC}}} \quad (1.53)$$

Equation (1.49) requires the evaluation of the derivative of the current with respect to the voltage. By writing the right term of (1.53) as $f(I,V)$, it is

$$\frac{dP}{dV} = I_{MPP} + V_{MPP} \frac{\frac{\partial}{\partial V} f(I,V)}{1 - \frac{\partial}{\partial I} f(I,V)} \quad (1.54)$$

Thus it results that

$$I_{MPP,STC} + V_{MPP,STC} \cdot \frac{-\dfrac{1}{R_p} - \dfrac{\left(I_{SC,STC} - \dfrac{V_{OC,STC} - R_s \cdot I_{SC,STC}}{R_p}\right) e^{\frac{V_{MPP,STC} + R_s \cdot I_{MPP,STC} - V_{OC,STC}}{\eta V_{t,STC}}}}{\eta V_{t,STC}}}{1 + \dfrac{\left(I_{SC,STC} - \dfrac{V_{OC,STC} - R_s \cdot I_{SC,STC}}{R_p}\right) e^{\frac{V_{MPP,STC} + R_s \cdot I_{MPP,STC} - V_{OC,STC}}{\eta V_{t,STC}}}}{\eta V_{t,STC}} + \dfrac{R_s}{R_p}} = 0$$

$$(1.55)$$

Finally, condition (1.50) can be rewritten as follows:

$$-\frac{1}{R_p} = \frac{-\dfrac{1}{R_p} - \dfrac{\left(I_{SC,STC} - \dfrac{V_{OC,STC} - R_s \cdot I_{SC,STC}}{R_p}\right) e^{\frac{V_{MPP,STC} + R_s \cdot I_{MPP,STC} - V_{OC,STC}}{\eta V_{t,STC}}}}{\eta V_{t,STC}}}{1 + \dfrac{\left(I_{SC,STC} - \dfrac{V_{OC,STC} - R_s \cdot I_{SC,STC}}{R_p}\right) e^{\frac{V_{MPP,STC} + R_s \cdot I_{MPP,STC} - V_{OC,STC}}{\eta V_{t,STC}}}}{\eta V_{t,STC}} + \dfrac{R_s}{R_p}} \quad (1.56)$$

The system of nonlinear equations made of (1.53), (1.55), and (1.56) must be solved numerically in order to determine R_s, R_p, and η.
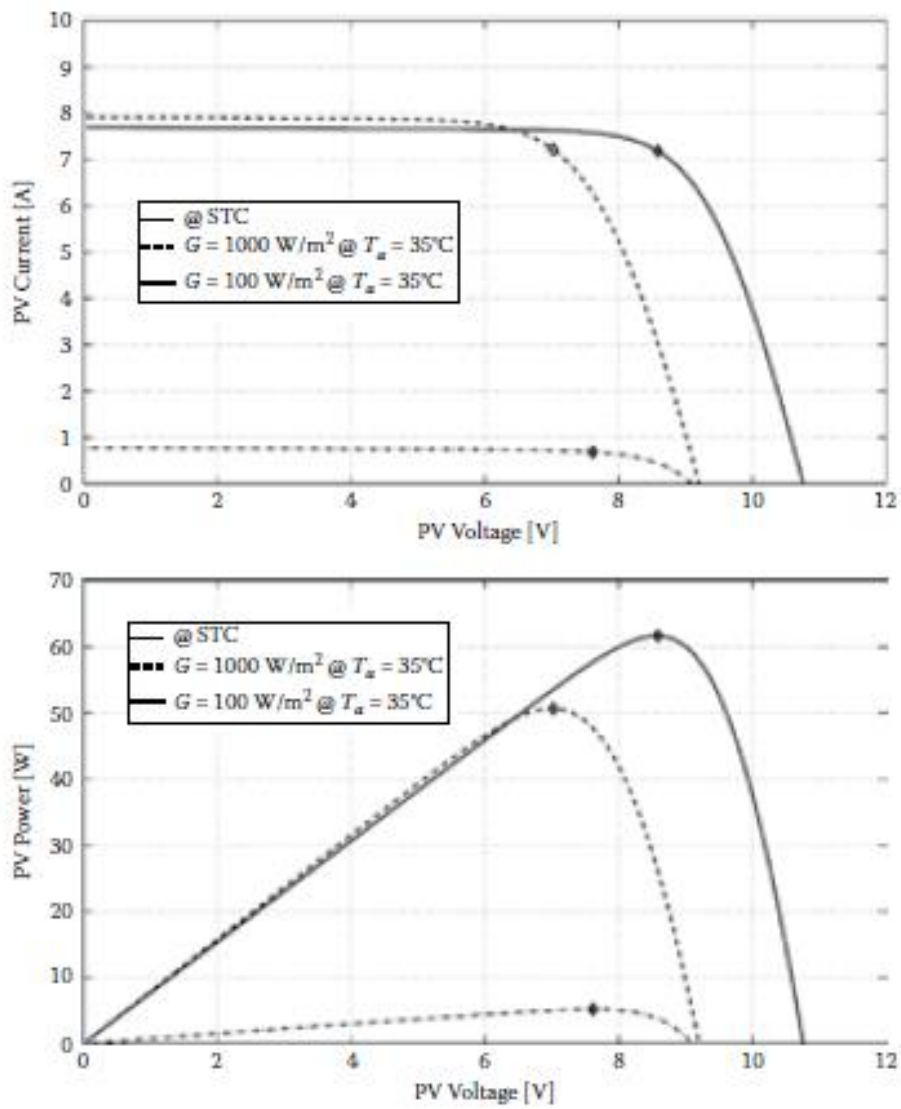
FIGURE 1.11
Current vs. voltage and power vs. voltage curves of a string of PV cells in STC and outdoor environmental conditions.

1.6.2 Modeling a Mismatched PV Generator

As discussed in the preceding sections, mismatching conditions occur when a part of the PV generator works in conditions that are different from those of the remaining part of the generator itself. The occurrence of this situation is due to shadowing or to a significant difference in the physical parameters characterizing the cells. Some approaches have been presented in literature, e.g., in [7, 12, 13], to analyze such situations.

The analysis approach discussed in this section refers to a single PV string made of a number of PV modules connected in series. Each PV module is supposed to be a number of equal cells connected in series and working in the same temperature and irradiance conditions. The cells in the PV module are supposed to be protected by a bypass diode connected in antiparallel, as in Figure 1.1. The approach can be applied to any number of strings connected in parallel.

The group of cells in each module, working in homogeneous conditions, is represented by the equivalent circuit in Figure 1.8 and modeled by the corresponding equation (1.10). Nevertheless, the modules in the string are characterized by different sets of parameters, accounting for nonuniformities in terms of irradiance, temperature, or manufacturing tolerances. In order to have a compact model, it is useful to embed the bypass diode model in a complete model describing the whole PV module, including the cells and the bypass diode, as shown in Figure 1.15.
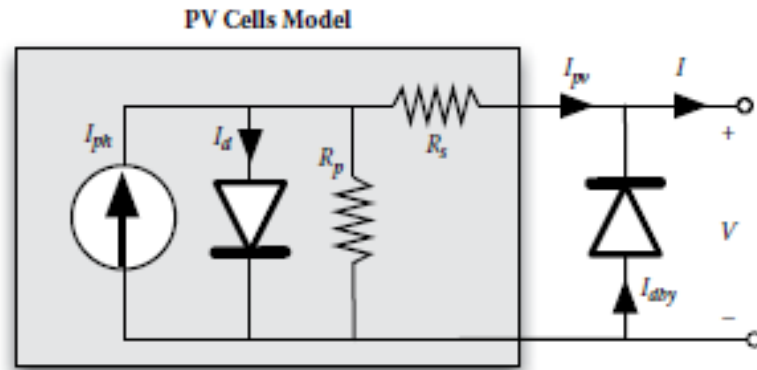
PV Cells Model

FIGURE 1.15
Equivalent circuit of a PV module with its own bypass diode.

The nonlinear characteristic equation of the bypass diode is given by the Shockley equation:

$$I_{dby} = I_{sat,dby}\left(e^{\frac{V}{\eta_{dby}V_{t,dby}}} - 1\right) \tag{1.59}$$

Merging (1.10) and (1.59) provides the following nonlinear and implicit equation:

$$I = I_{ph} - I_{sat}\left[e^{\frac{V+I\cdot R_s}{\eta V_t}} - 1\right] - \frac{V+I\cdot R_s}{R_p} + I_{sat,dby}\left(e^{\frac{V}{\eta_{dby}V_{t,dby}}} - 1\right) \tag{1.60}$$

Once again, the Lambert W function is useful to put (1.60) into explicit form. The whole module, including the group of cells and the bypass diode, is then described by the following explicit equation, which gives the value of the current of the building block shown in Figure 1.15 as a function of the voltage at its terminals:

$$I = \frac{\left[R_p\left(I_{ph} + I_{sat}\right) - V\right]}{R_s + R_p} + I_{sat,dby}\left(e^{\frac{V}{\eta_{dby}V_{t,dby}}} - 1\right) - \frac{\eta V_t}{R_s}lambertW(\theta) \tag{1.61}$$

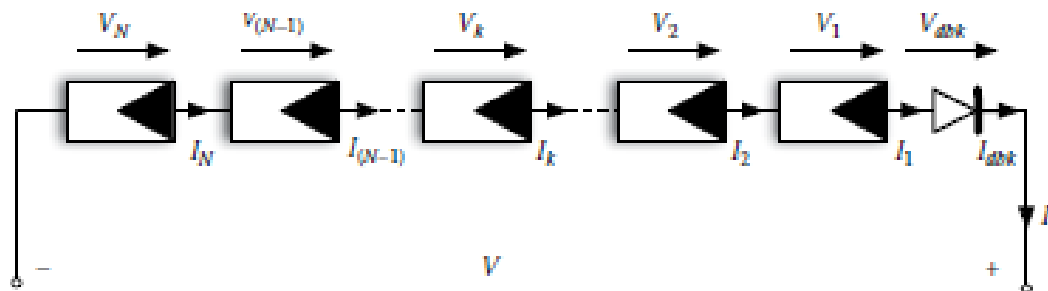**FIGURE 1.16**
String of PV modules with blocking diode.

$$\begin{cases} V_1 + V_2 + \cdots + V_k + \cdots + V_{N-1} + V_N + V_{dbk} - V = 0 \\ I_1(V_1) - I_2(V_2) = 0 \\ I_1(V_1) - I_3(V_3) = 0 \\ \cdots \\ I_1(V_1) - I_k(V_k) = 0 \\ \cdots \\ I_1(V_1) - I_{N-1}(V_{N-1}) = 0 \\ I_1(V_1) - I_N(V_N) = 0 \\ I_1(V_1) - I_{dbk}(V_{dbk}) = 0 \end{cases}$$ (1.62)

$$I_{dbk} = I_{sat,dbk} \cdot \left(e^{\frac{V_{dbk}}{V_{t,dbk}}} - 1 \right)$$
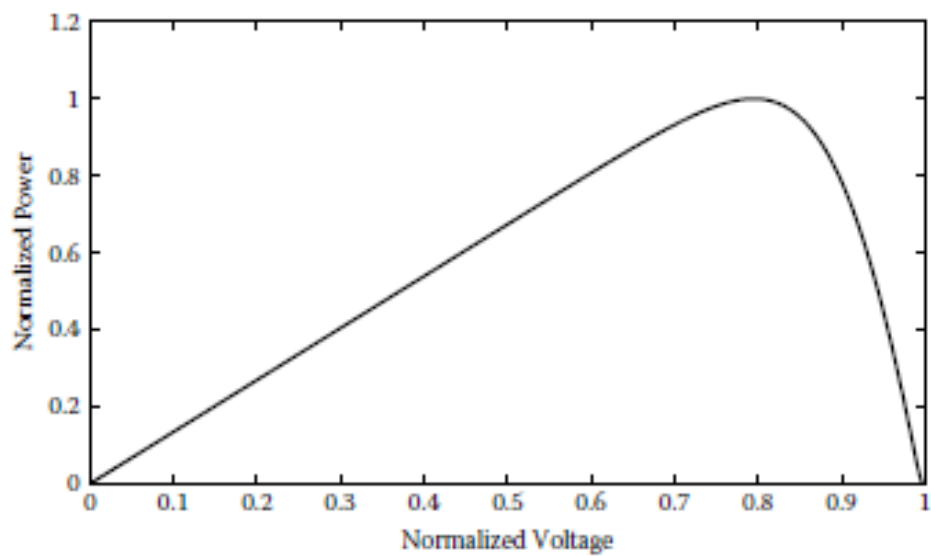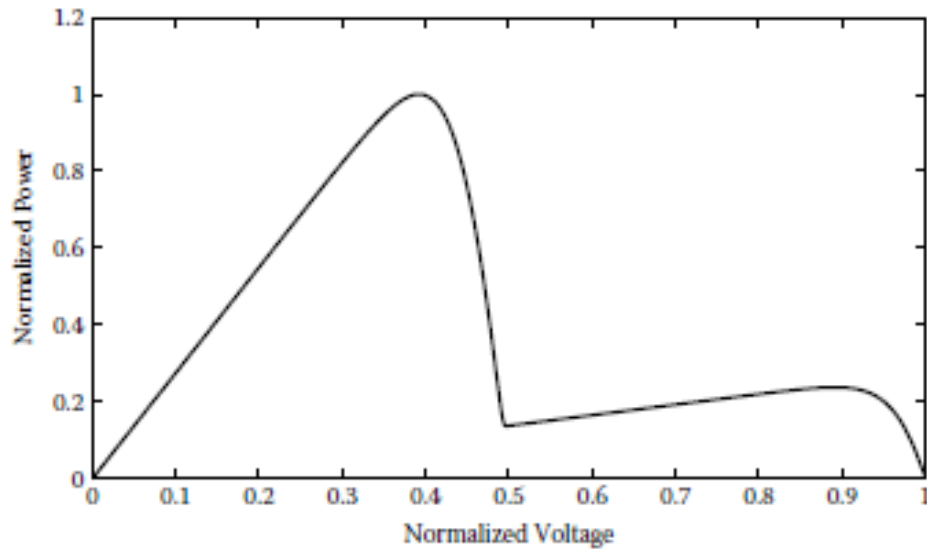

FIGURE 1.17
PV characteristic in uniform conditions.

FIGURE 1.18
P-V characteristic in mismatched conditions.

Maximum Power Point Tracking

2.1 The Dynamic Optimization Problem

The same conclusion holds if the PV array feeds a resistive load, because the intersection between the resistor characteristic and the I-V curve of the PV array cannot always occur in the MPP for the whole day, so that a power lower than the maximum one is delivered to the load. Figures 2.1 and 2.2 show that the operating point resulting from a straightforward connection of a PV generator with a battery or a resistive load cannot be the MPP in any irradiance or temperature condition.

As a consequence, it is mandatory to adopt an intermediate conversion stage, interfacing the PV array and the power system that processes or uses the electrical power produced thereof, which must be capable of adapting its input voltage and current levels to the instantaneous PV source MPP, while keeping its output voltage and current levels compliant with the load requirement. Such a stage must be a *dynamical optimizator*, which means that it must
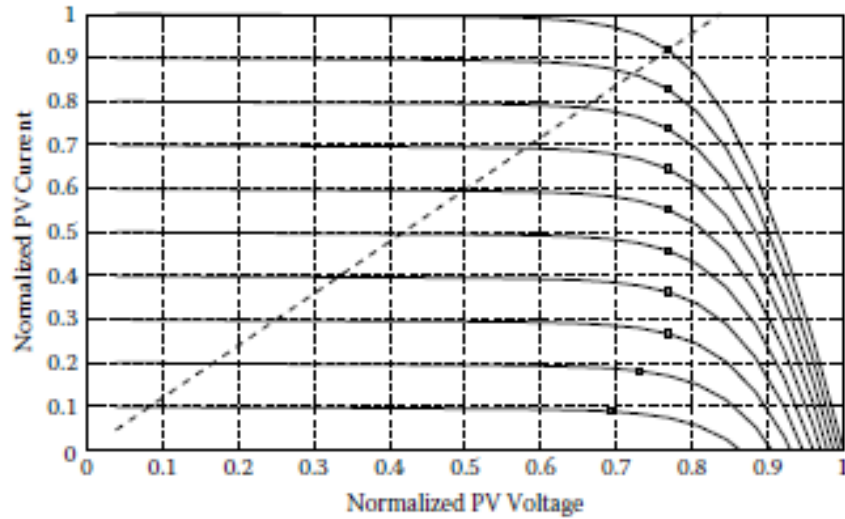
FIGURE 2.1
Operating conditions resulting from a straight connection of a PV generator with a resistive load at varying irradiance levels. Squares are the MPPs.

be able to perform this adaptation in the presence of time-varying operating conditions affecting the PV generator. The adoption of a linear regulator would be ineffective from the efficiency point of view, so that a switching converter is almost always employed. Because of the reduced cost of power devices, the adoption of a switching converter is now in use from very low power levels, e.g., energy scavenging, up to high power applications, e.g.,
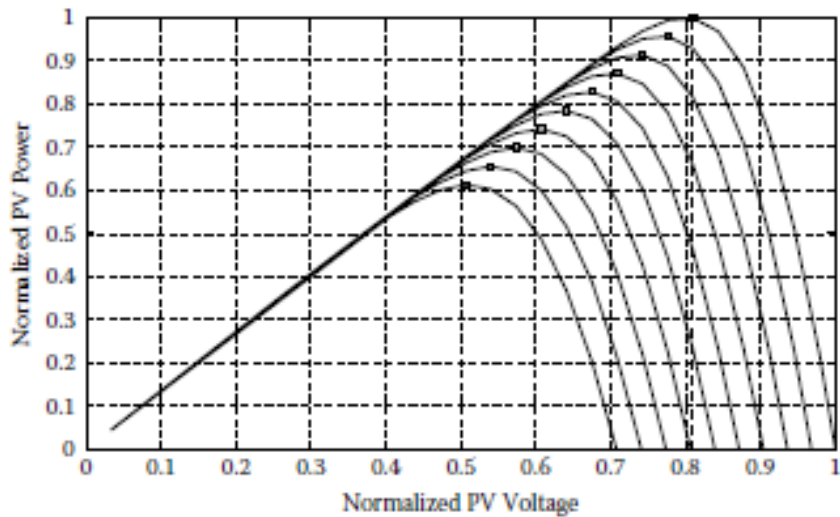
FIGURE 2.2
Operating conditions resulting from a straight connection of a PV generator with a battery at varying temperatures. Squares are the MPPs.

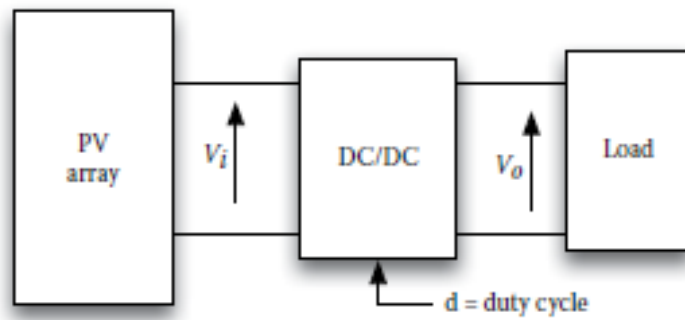$$R_{in}(d) = \frac{R_{Load}}{M(d)^2}; \qquad V_i(d) = \frac{V_o}{M(d)} \qquad (2.1)$$

FIGURE 2.3
Connection scheme of a DC/DC converter dedicated to the dynamical optimization of a PV generator.
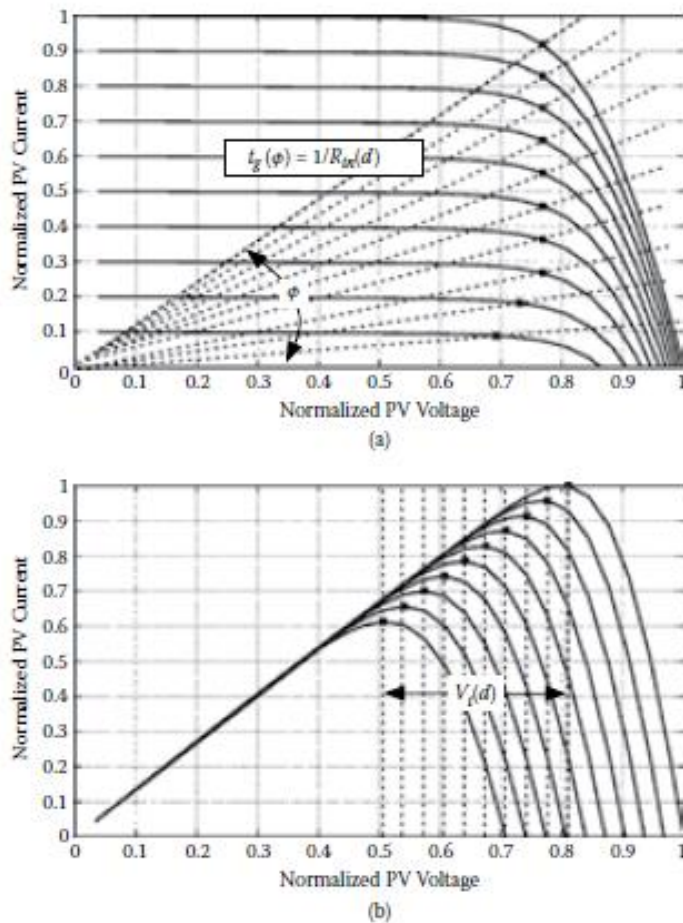

FIGURE 2.4
Operating conditions resulting from a PV generator interfaced to a DC/DC converter. In (a) the PV source has been characterized for different irradiance levels, and in (b) the PV source has been characterized for different temperature levels.
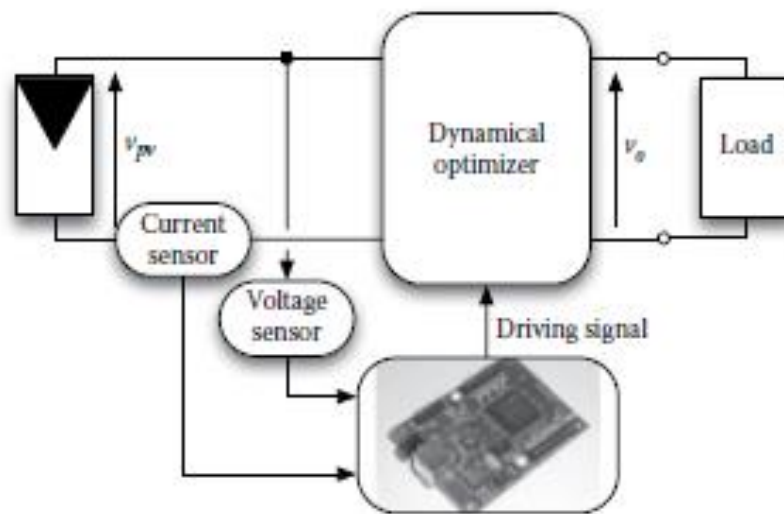
FIGURE 2.5
MPPT implementation.

2.4 The Perturb and Observe Approach

The perturb and observe (P&O) method is the most popular algorithm belonging to the class of the *direct MPPT* techniques; it is characterized by the injection of a small perturbation into the system, whose effects are used to drive the operating point toward the MPP. Other methods derived by the P&O approach are the incremental conductance (INC), the self-oscillation (SO) method, and the extremum seeking (ES) control. Such methods differ from the P&O approach either for the variable observed or for the type of perturbation. All these algorithms have the advantage of being independent of the knowledge of the PV generator characteristics, so that the MPP is tracked regardless of the irradiance level, temperature, degradation, and aging, thus ensuring high robustness and reliability.

The first use of the P&O technique for tracking the MPP in PV systems goes back to the 1970s, when it was used intensively for aerospace applications [7]. At that time a fully analog implementation was adopted; nowadays, with the progress of the performances of low-cost microcontrollers, the digital implementation is preferred because the implementation of the MPPT algorithm results in a simple code [8].

The P&O method is based on the following concept: The PV operating point is perturbed periodically by changing the voltage at PV source terminals, and after each perturbation, the control algorithm compares the values of the power fed by the PV source before and after the perturbation. If after the perturbation the PV power has increased, this means that the operating point has been moved toward the MPP; consequently, the subsequent perturbation imposed to the voltage will have the same sign as the previous one. If after a voltage perturbation the power drawn from the PV array decreases, this means that the operating point has been moved away from the MPP.
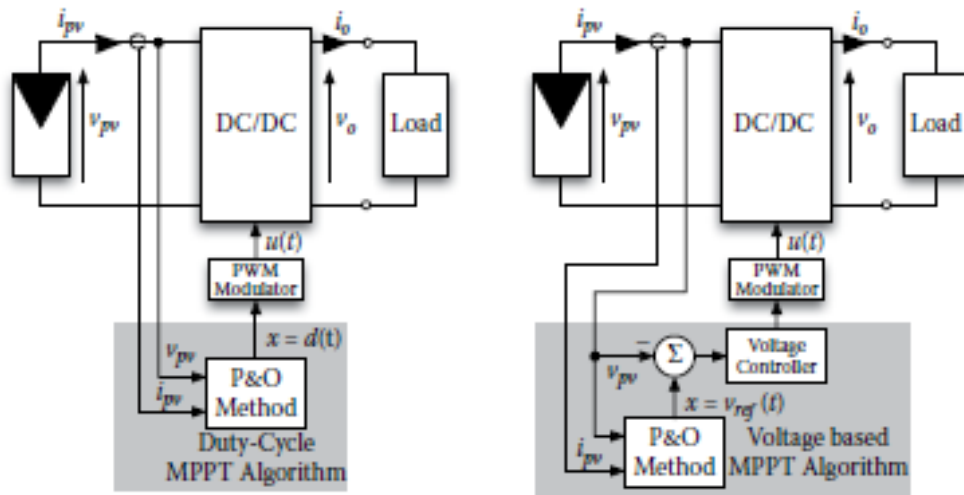
FIGURE 2.6
Basic schemes for implementing the P&O algorithm.

Therefore the sign of the subsequent voltage perturbation is reversed. The switching converter is used to drive the perturbation of the operating voltage of the PV generator.

Two basic P&O configurations can be adopted for controlling the switching converter and realizing the PV source voltage perturbation: The first one involves a direct perturbation of the duty ratio of the power converter. In the second one the perturbation is applied to the reference voltage of an error amplifier that generates the signal controlling the duty cycle. Both solutions are shown in Figure 2.6. In the first case, the converter operates in open loop after each duty cycle perturbation, while in the second case the converter is equipped with a feedback voltage loop.

The general equation describing the P&O algorithm is

$$x_{((k+1)T_p)} = x_{(kT_p)} \pm \quad x = x_{(kT_p)} + (x_{(kT_p)} - x_{((k-1)T_p)}) \cdot sign(P_{(kT_p)} - P_{(k-1)T_p)}) \quad (2.2)$$
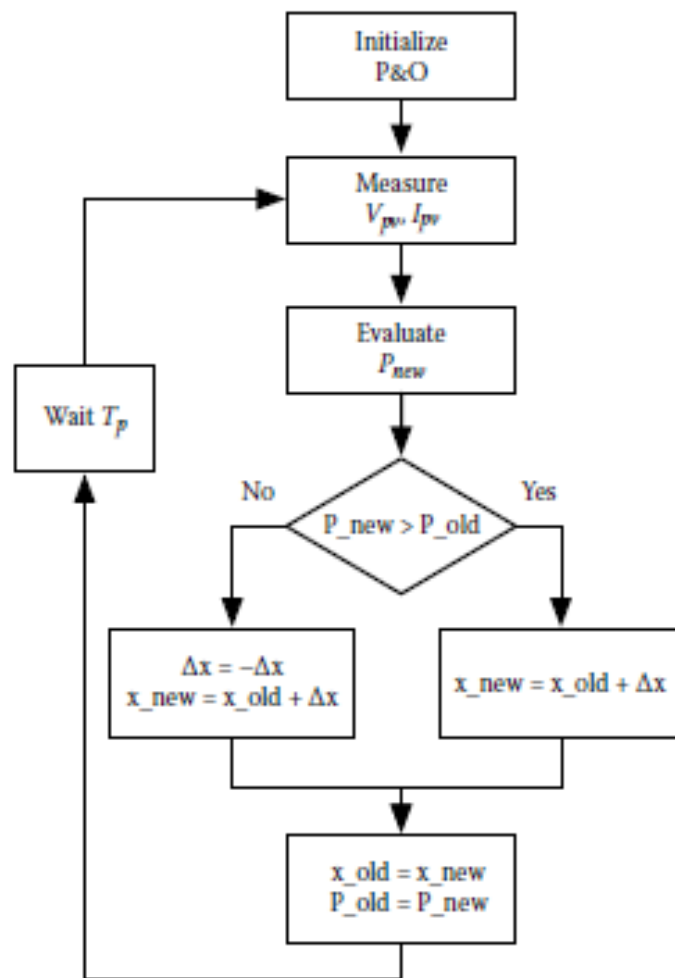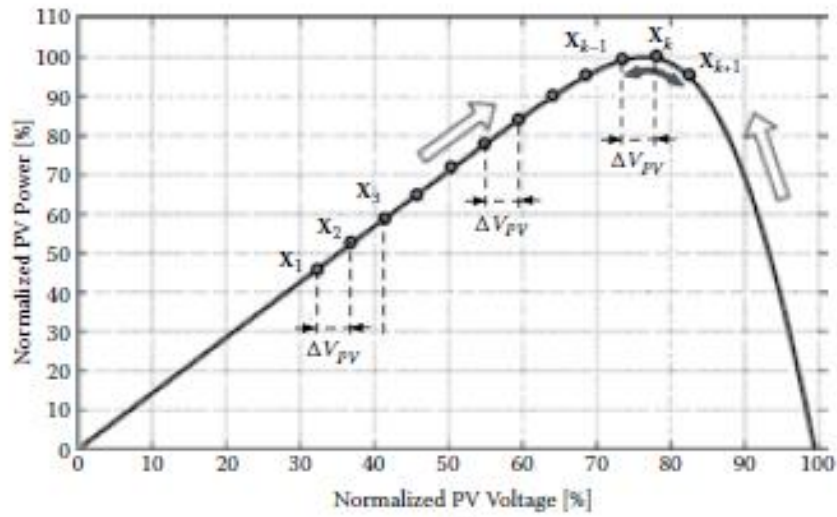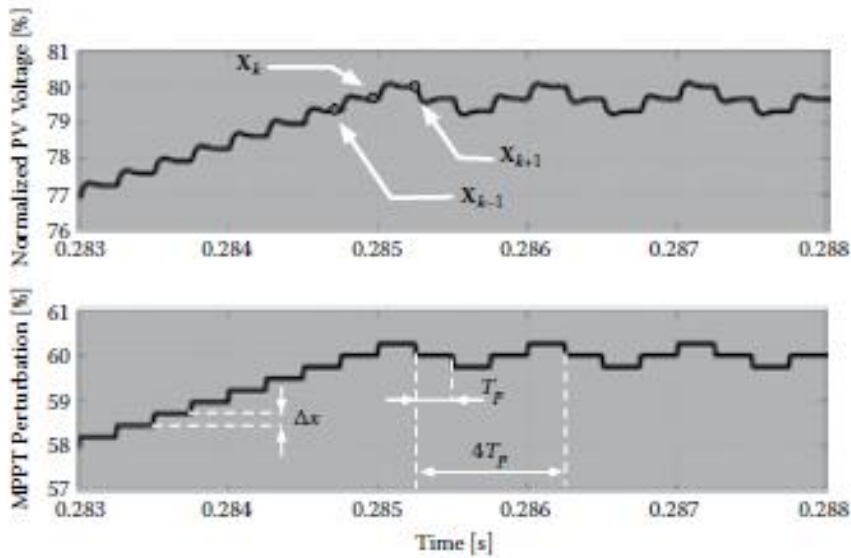
FIGURE 2.7
Basic flowchart for implementing the P&O algorithm.

FIGURE 2.8
PV operating points imposed by the P&O algorithm. (a) Power vs. voltage characteristic. (b) Time domain behavior.

$$G_{vp,x}(s) = \frac{\hat{v}_{PV}(s)}{\hat{x}(s)} = \frac{\mu \cdot \omega_n^2}{s^2 + 2\zeta \cdot \omega_n \cdot s + \omega_n^2} \qquad (2.15)$$

where μ is the static gain, ω_n is the natural frequency, and ζ is the damping factor of a canonical second-order system.
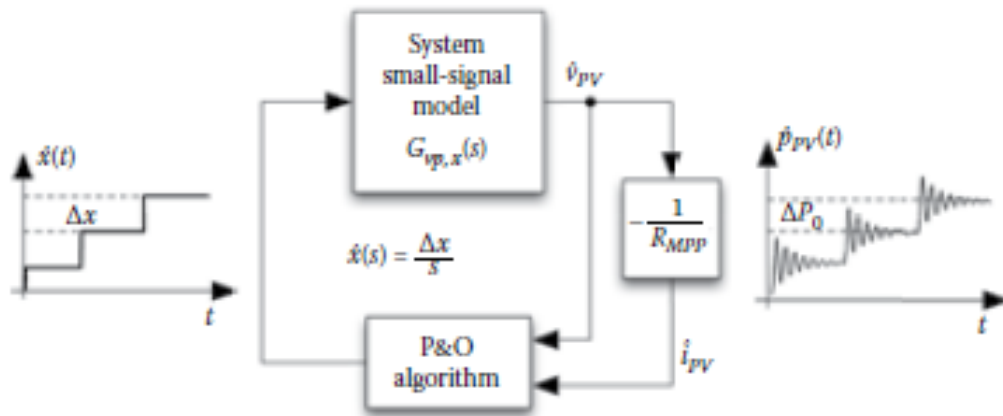

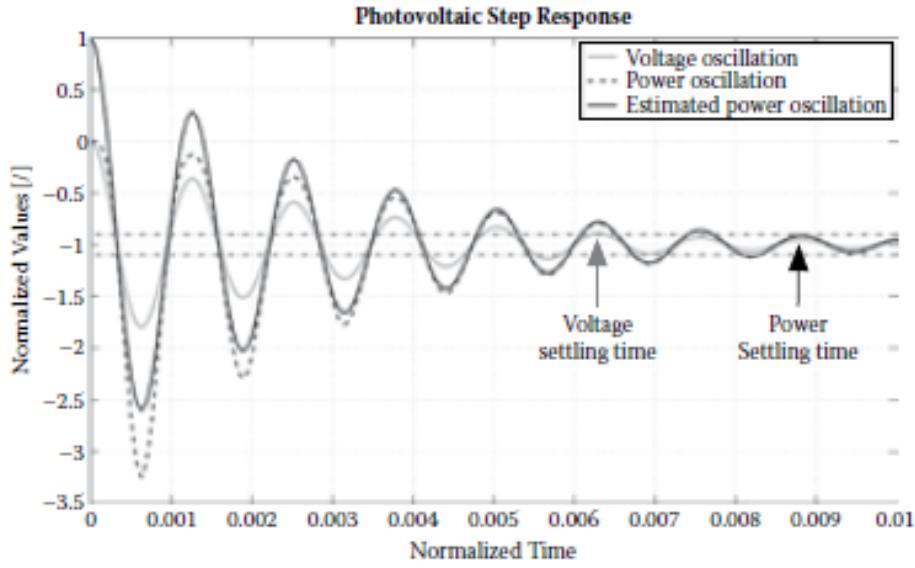**FIGURE 2.9**
Model for PV dynamic behavior analysis.

Photovoltaic Step Response

FIGURE 2.10
PV power dynamic behavior.

Evaluating the envelope of (2.17) in the T_ε yields

$$P_0 \cdot (1+\varepsilon) \simeq P_0 \left(1 - \frac{2}{\sqrt{1-\zeta^2}} e^{-\zeta \omega_n T_\varepsilon} \right) \tag{2.20}$$

so that the following expression of the settling time T_ε is obtained:

$$T_\varepsilon \simeq -\frac{1}{\zeta \cdot \omega_n} ln(\varepsilon / 2) \tag{2.21}$$

It is worth noting that, with the same boundary value ε, the 1/2 factor in (2.21) makes the settling time of the PV power oscillation considerably different with respect to that of the PV voltage oscillation. For the example proposed in Figure 2.10, it is more or less 30% higher than the PV voltage settling time.

Based on the previous modeling results, the MPPT is not affected by mistakes caused by transient oscillations of the PV system caused by its own action if the following condition is fulfilled:

$$T_P \geq T_J \simeq -\frac{1}{\zeta \cdot \omega_n} ln(J / 2) \bigg|_{J=0.1} \tag{2.22}$$

where the value $\varepsilon = 0.1$ is chosen according to the classical control system theory.

2.4.3 P&O Design Example: A PV Battery Charger

Guidelines for designing the P&O algorithm based on the duty cycle pertur-
bation are analyzed in this section. Figure 2.12 shows the basic scheme of a
PV battery charger based on a boost DC/DC converter. An additional control
circuitry, providing battery over voltage and over current protections, which
must be considered in the practical application, has no effect on the MPPT
design procedure.

As explained in Section 2.4.1, the first step is to identify the control-to-PV
voltage transfer function: In the case under study the MPPT acts on the duty
cycle directly so that $G_{vp,x}(s) = \hat{v}_{PV} / \hat{x}$ corresponds to $G_{vp,d}(s) = \hat{v}_{PV} / \hat{d}$. The
scheme of Figure 2.13 shows the whole small-signal model of the PV battery
charger that can be used to evaluate $G_{vp,d}(s)$.

As steady-state environmental conditions are supposed, the small-signal
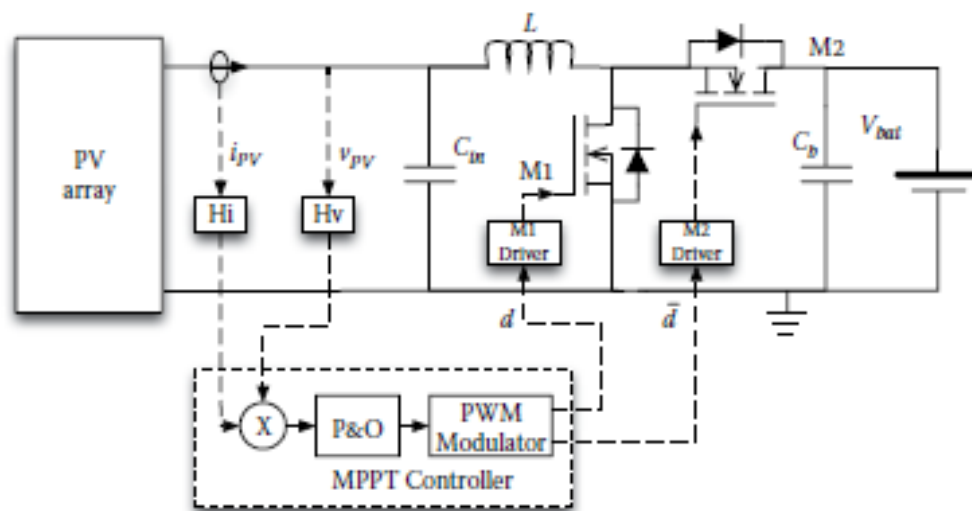model of the PV field is given by its differential resistance obtained by using

FIGURE 2.12
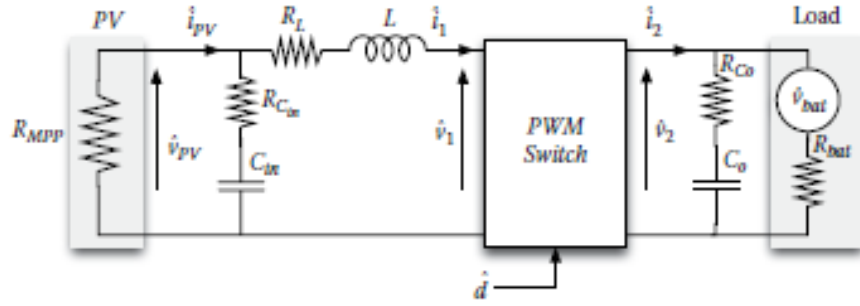PV battery charger with a boost converter.

FIGURE 2.13
Small-signal model of PV battery charger.

(2.5) in the MPP. The DC/DC converter, instead, is decoupled in its linear parts and in a linearized small-signal part [12] modeled by the following equations:

$$\begin{cases} \hat{i}_2 = (1-D)\cdot\hat{i}_1 - I_1\cdot\hat{d} \\ \hat{v}_1 = (1-D)\cdot\hat{v}_2 - V_2\cdot\hat{d} \end{cases}$$

(2.37)

which completely describe the block *PWM SWITCH* shown in the scheme of Figure 2.13 and deeply analyzed in [12]. The additional small-signal source $\hat{v}_{bat}$ is used to model the low-frequency variations at the converter's output caused by load changes.

The oscillations $\hat{v}_{bat}$ can propagate up to the PV terminals, thus causing a possible deceiving effect on the operation of the MPPT algorithm, because it might be unable to distinguish the PV voltage oscillations caused by $\hat{v}_{bat}$ with respect to the PV voltage oscillations introduced by the perturbation of the duty cycle $\hat{d}$. In this example the battery is considered an ideal voltage source; thus $\hat{v}_{bat} = 0$, $R_{bat} = 0$. The problems related to the disturbances coming from the converter output will be investigated in depth in Chapter 3.

In this example the main parasitic parameters of the DC/DC converter have been also accounted for; nevertheless, $G_{vp,d}(s)$ assumes an expression similar to (2.15):

$$G_{vp,d}(s) = \frac{\mu \cdot \omega_n^2 \left(1 + \dfrac{s}{\omega_z}\right)}{s^2 + 2\zeta\cdot\omega_n\cdot s + \omega_n^2}$$

(2.38)

where

$$\mu = -V_{bat} \quad \omega_n = \frac{1}{\sqrt{L\cdot C_{in}}} \quad \omega_z = \frac{1}{R_{C_{in}}\cdot C_{in}}$$

(2.39)

$$\zeta = \frac{1}{2\cdot R_{MPP}}\sqrt{\frac{L}{C_{in}}} + \frac{R_{C_{in}} + R_L}{2}\sqrt{\frac{C_{in}}{L}}$$
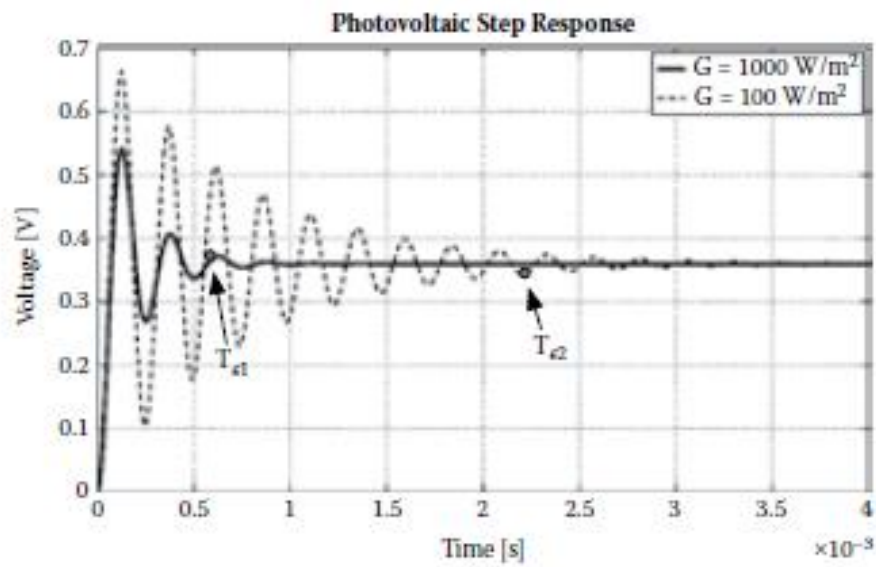
(2.40)

FIGURE 2.14
Settling time evaluation for the PV battery charger.
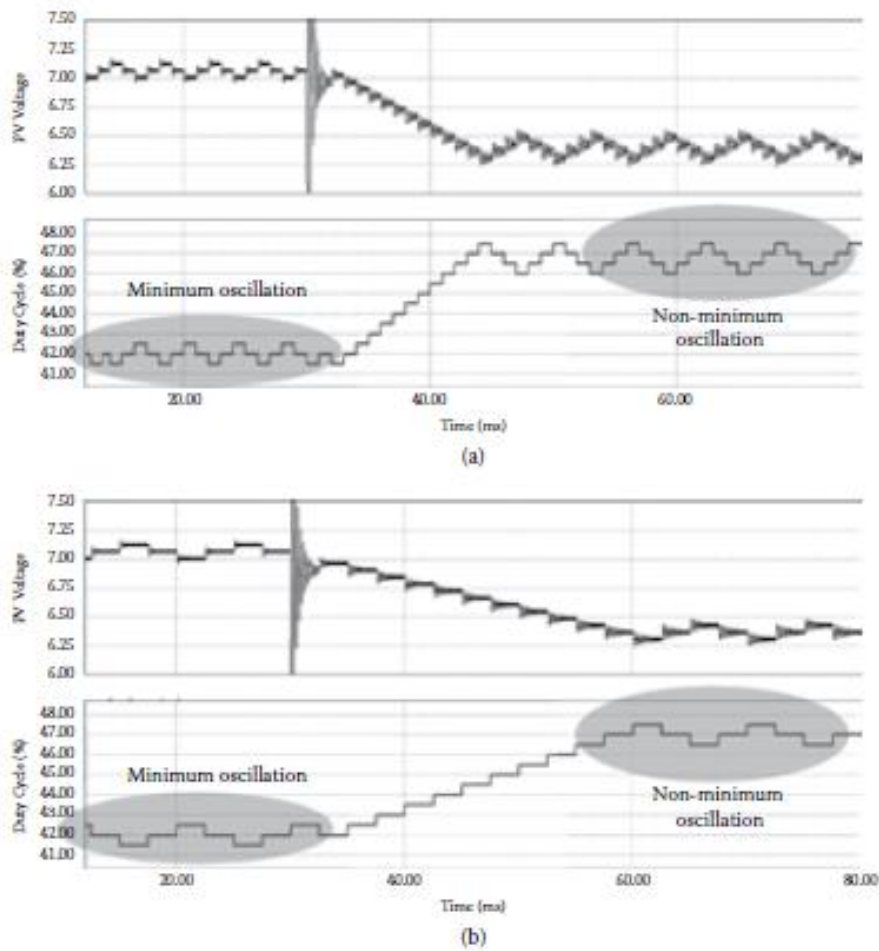

(a)

(b)

FIGURE 2.15
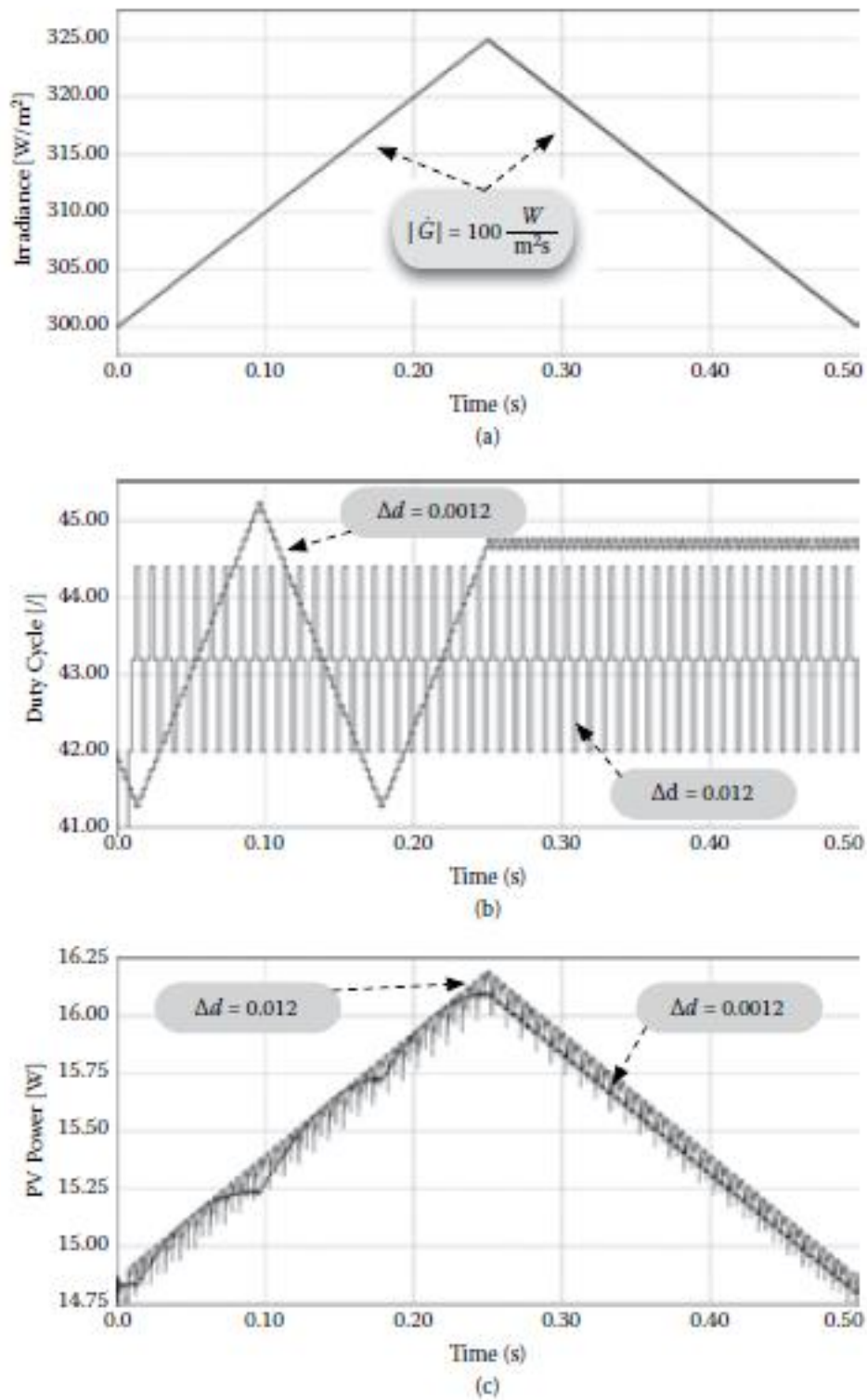P&O behavior in steady-state environmental conditions.

FIGURE 2.16
P&O behavior in dynamic environmental conditions. (a) Irradiance profile. (b) Duty cycle variations. (c) Instantaneous PV power.

2.5.2 P&O with Parabolic Approximation

In [18] it is shown that a parabolic interpolation based on the last three sampled voltage-power couples allows us to balance the position of the three
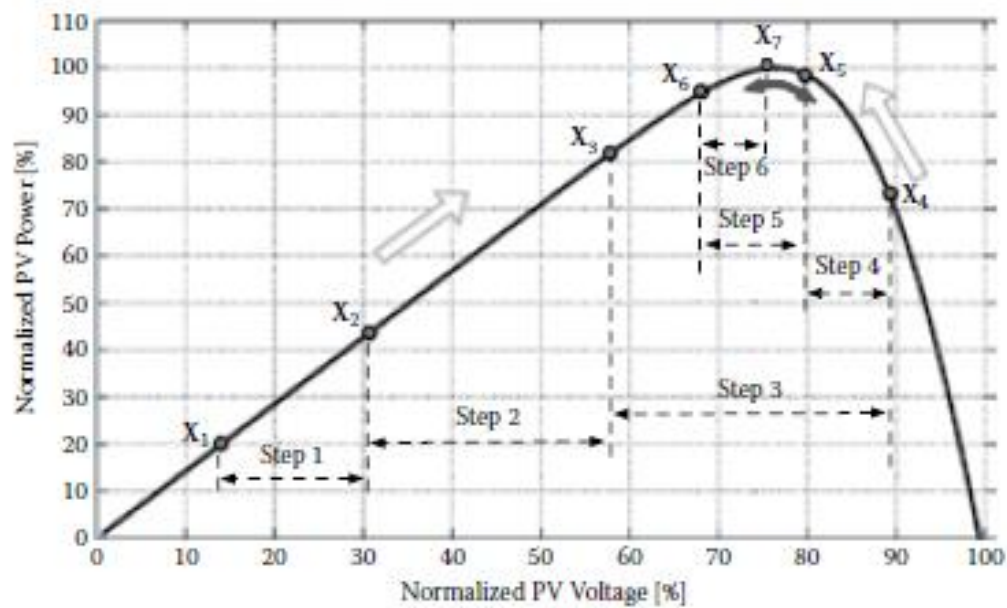

FIGURE 2.18
Variable step MPPT.

$$p_{PV} = \alpha \cdot v_{PV}^2 + \beta \cdot v_{PV} + \gamma \qquad (2.47)$$

with $\alpha < 0$ and the vertex at $v_{peak} = -\beta/(2\alpha)$, with $p_{peak} = \gamma - \beta^2/(4\alpha)$.

If the P-V curve and the interpolating parabola have at least three points in common, the coefficients α, β, and γ can be determined by solving the following system of equations:

$$\begin{cases} p_1 = \alpha \cdot v_1^2 + \beta \cdot v_1 + \gamma \\ p_2 = \alpha \cdot v_2^2 + \beta \cdot v_2 + \gamma \\ p_3 = \alpha \cdot v_3^2 + \beta \cdot v_3 + \gamma \end{cases} \qquad (2.48)$$

A first-in/first-out array containing the actual operating point and the preceding two, corresponding to the couple of values $[(p_1,v_1) - (p_2,v_2) - (p_3,v_3)]$, is used to find the interpolating parabola. Once such an approximation is obtained, the vertex of the parabola is used as a prediction of the new operating point, as shown in Figure 2.22.

The interpolating parabola is considered misleading in the MPPT process if it exhibits an upward-turned concavity, or if it has a vertex at a voltage
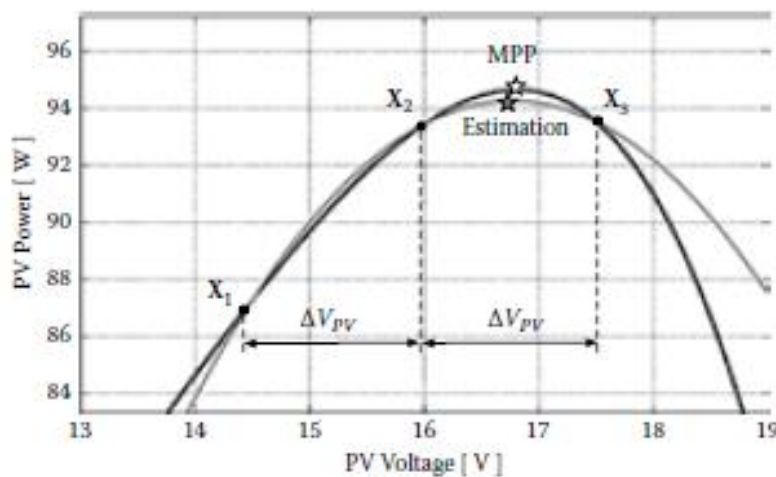

FIGURE 2.22
MPP estimation by means of parabolic (red curve) interpolation.

Read Page 70 to 84 Other methods and techniques

3

MPPT Efficiency: Noise Sources and Methods for Reducing Their Effects

3.1 Low-Frequency Disturbances in Single-Phase Applications

AC applications of PV systems require a power processing element able to convert the DC power generated by the PV unit into AC power, at 110 or 230 V rms voltage rating by adapting the PV voltage to that needed by the stage performing DC/AC conversion. The adoption of single-stage power processing units is the best choice, especially from the point of view of reliability and efficiency. Some commercial solutions, especially in the power range of interest for residential power plants (e.g., from Fronius and SMA), are based on the topology depicted in Figure 3.1, which consists of only a pulse-width modulation (PWM) inverter controlled in such a way that the maximum power from the PV source is extracted and an almost pure sinusoidal current is injected into the grid or into an AC stand-alone system with energy backup.

Because of the inherent step-down characteristic of the inverting bridge, the adoption of a single-stage inverter requires that the PV voltage be higher than the peak AC voltage value, so that this solution is not suitable for low-power PV applications like microinverters.

Double-stage or multiple-stage solutions are based on a DC/DC converter that controls the PV source and performs the MPPT function, cascaded by a DC/AC conversion stage. Such architecture is shown in Figure 3.2, where the bulk capacitance, placed between the two conversion stages, plays an important role.

The bulk capacitance, indeed, handles the imbalance between the PV power made available at the DC bus by the DC/DC stage and the AC power absorbed by the grid through the DC/AC stage. The difference between the DC power and the AC power is a sinusoidal component at twice the AC grid frequency, namely, either 100 or 120 Hz, as shown in Figures 3.2 and 3.3. The amplitude of the voltage oscillation across the bulk capacitor due to the AC
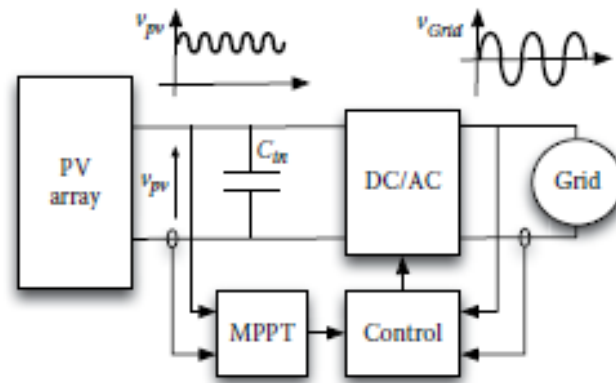
FIGURE 3.1
Single-stage, single-phase PV inverter.

power component can be easily calculated by assuming that the bulk capacitor current has the following expression:

$$i_b(t) = I_b \cdot \cos(2 \cdot \omega_{grid} \cdot t) \tag{3.1}$$

where ω_{grid} is the grid frequency. The AC component of the bulk voltage is then given by

$$\hat{v}_b(t) = \frac{I_b}{C_b} \cdot \int_{T_{grid}} \cos\left(2 \cdot \omega_{grid} \cdot t\right) dt = \frac{I_b}{2 \cdot \omega_{grid} \cdot C_b} \sin\left(2 \cdot \omega_{grid} \cdot t\right) \tag{3.2}$$
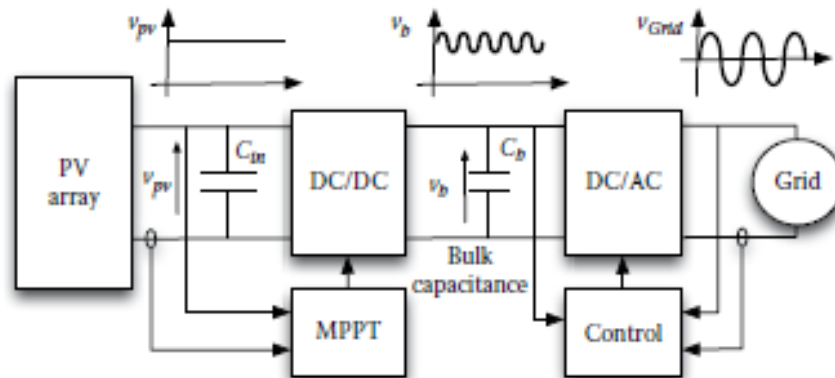

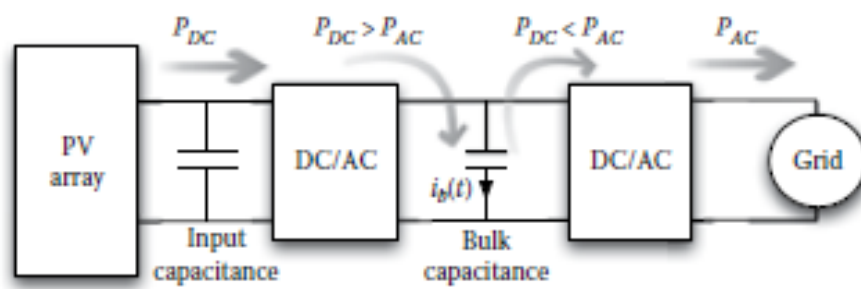**FIGURE 3.2**
Double-stage, single-phase PV inverter.

FIGURE 3.3
Role of the bulk capacitance.

and the peak-to-peak value of the voltage oscillation at a frequency $2 \cdot \omega_{grid}$ is

$$V_b = \frac{P_{PV}}{2 \cdot \omega_{grid} \cdot C_b \cdot V_b} \qquad (3.3)$$

lel resistances in the PV array model provides the following PV MPP current and relevant derivatives:

$$I_{MPP} = I_{ph} - I_0 \left(e^{\frac{V_{MPP}}{\eta \cdot V_T \cdot n_s}} - 1 \right) \tag{3.4}$$

$$\frac{\partial I_{MPP}}{\partial V_{MPP}} = -\frac{I_0}{\eta \cdot V_T \cdot n_s} \cdot e^{\frac{V_{MPP}}{\eta \cdot V_T \cdot n_s}} \tag{3.5}$$

$$\frac{\partial^2 I_{MPP}}{\partial V_{MPP}^2} = -\frac{I_0}{(\eta \cdot V_T \cdot n_s)^2} \cdot e^{\frac{V_{MPP}}{\eta \cdot V_T \cdot n_s}} \tag{3.6}$$

These expressions allow us to approximate the PV current vs. voltage curve across the MPP by means of the second-order Taylor series:

$$i_{PV} = I_{MPP} + \frac{\partial I_{MPP}}{\partial V_{MPP}}(v_{PV} - V_{MPP}) + \frac{\partial^2 I_{MPP}}{\partial V_{MPP}^2} \cdot (v_{PV} - V_{MPP})^2 \tag{3.7}$$

that is,

$$i_{PV} = \gamma + \beta \cdot v_{PV} + \alpha \cdot v_{PV}^2 \tag{3.8}$$

where

$$\gamma = I_{MPP} - V_{MPP} \frac{\partial I_{MPP}}{\partial V_{MPP}} + \frac{1}{2} \frac{\partial^2 I_{MPP}}{\partial V_{MPP}^2} V_{MPP}^2 \tag{3.9}$$

$$\beta = \frac{\partial I_{MPP}}{\partial V_{MPP}} - V_{MPP} \cdot \frac{\partial^2 I_{MPP}}{\partial V_{MPP}^2} \tag{3.10}$$

$$\alpha = \frac{1}{2} \frac{\partial^2 I_{MPP}}{\partial V_{MPP}^2} \tag{3.11}$$

The oscillation of the bulk voltage causes an oscillation of the PV voltage across the MPP: If $M(D) = V_b/V_{PV}$ is the voltage conversion ratio of the DC/DC converter, then $\Delta V_{PV} = \Delta V_b/M(D)$. The PV voltage is thus given by

$$v_{PV}(t) = V_{MPP} + \hat{v}(t) = V_{MPP} + \quad V_{PV} \cdot sin(2\omega_{grid} \cdot t) \tag{3.12}$$
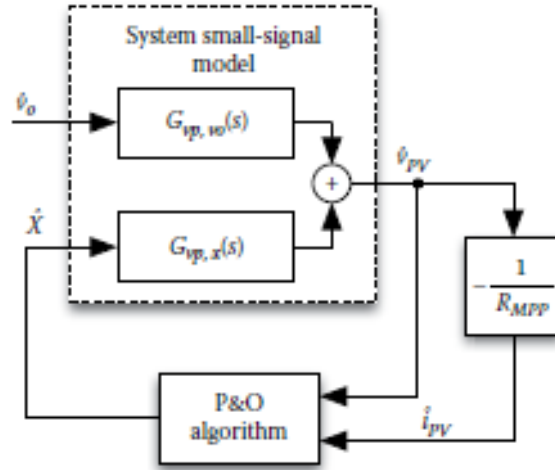
FIGURE 3.4
Effect of output voltage noise on the PV voltage.

performances. The benefits of the feedback compensation in the P&O operation will be analyzed, and an example of how to apply the P&O design equation to the closed-loop converters will be proposed.

The effect of the noise on the PV voltage is described by using the output-to-input $G_{vp,vo}(s)$ transfer function, as shown in Figure 3.4. In this scheme the converter transfer functions depend on the architecture selected for performing the MPPT.

Both the P&O perturbation ($\hat{x}$) and the output voltage noise ($\hat{v}_o$) affect the PV voltage. An estimation of the maximum ΔV_{PV} variation is

$$V_{PV} = |G_o \cdot x| + |G_{vp,vo}(\omega) \cdot V_o| \tag{3.16}$$

where the first term has already been introduced in (2.33) and represents the P&O effect, $G_{vp,vo}(\omega)$ is the magnitude of the output-to-input transfer function evaluated at the noise frequency ω, and ΔV_o is the amplitude of the output voltage noise (V_o). Equation (3.16) involves the absolute values because the signs of both voltage variations are not correlated and cannot be predicted in advance. The use of the absolute quantities ensures that we take into account the worst case for the ΔV_{PV} variation. As a consequence, by substituting eq. (3.16) in (2.32) we get

$$P_{PV} \simeq -\left(H \cdot V_{MPP} + \frac{1}{R_{MPP}} \right) \left(|G_o \cdot x| + |G_{vp,vo}(\omega) \cdot V_o| \right)^2 \tag{3.17}$$
$$+ V_{MPP} \cdot K_{pk} \ G$$

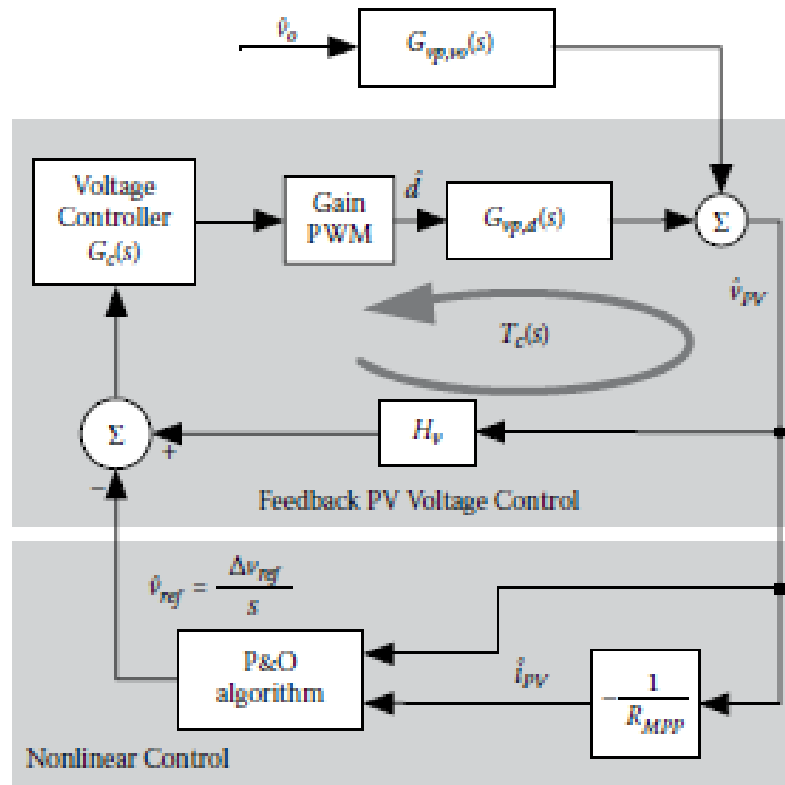where the symbols have the same meaning described in Section 2.4.2.

FIGURE 3.5
Small-signal model with a PV voltage compensation network.

The closed-loop transfer function $W_{vp,v_{ref}}(s)$, between $\hat{v}_{PV}(s)$ and $\hat{v}_{ref}(s)$, is

$$W_{vp,v_{ref}}(s) = \frac{\hat{v}_{PV}(s)}{\hat{v}_{ref}(s)} = \frac{1}{H_v}\frac{T_c(s)}{1+T_c(s)} \simeq \frac{1}{H_v} \tag{3.21}$$

3.1.2 Example of P&O Design for a Closed-Loop Boost Converter

Figures 3.6 and 2.12 show the same circuit, but the former one includes a 100 Hz voltage oscillation at the converter output and also the $G_c(s)$ compensation network.

The small-signal model shown in Figure 2.13 allows us to determine the following transfer function $G_{vp,vo}(s)$:

$$G_{vp,vo}(s) = \frac{\mu \cdot \omega_n^2 \left(1 + \dfrac{s}{\omega_z}\right)}{s^2 + 2\zeta \cdot \omega_n \cdot s + \omega_n^2} \tag{3.24}$$

with $\mu = 1 - D$ and all the other coefficients given in (2.39) and (2.40).

The linear compensation network is designed on the basis of the desired dynamic performances: Given the desired crossover frequency and the
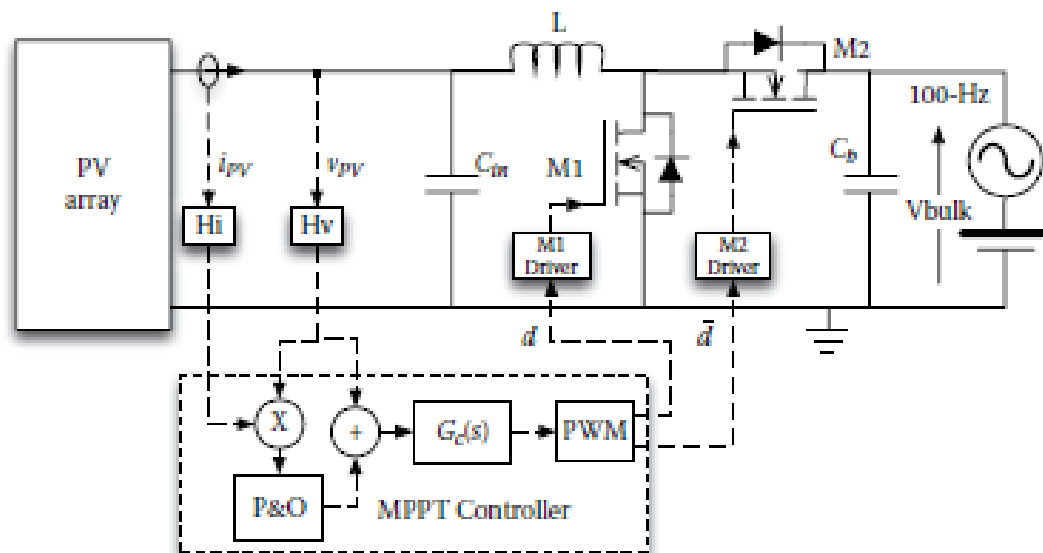

FIGURE 3.6
PV battery charger with a boost converter.

3.2 Instability of the Current-Based MPPT Algorithms

The largest part of the MPPT algorithms presented in literature and used in commercial products is based on the voltage-mode feedback control, or at least on a combination of control loops in which the final objective is to regulate the PV voltage. Indeed, the logarithmic dependency of the PV voltage on the irradiation level makes the MPPT algorithm based on the regulation of the PV voltage less sensible to the irradiance variation [13]. On the
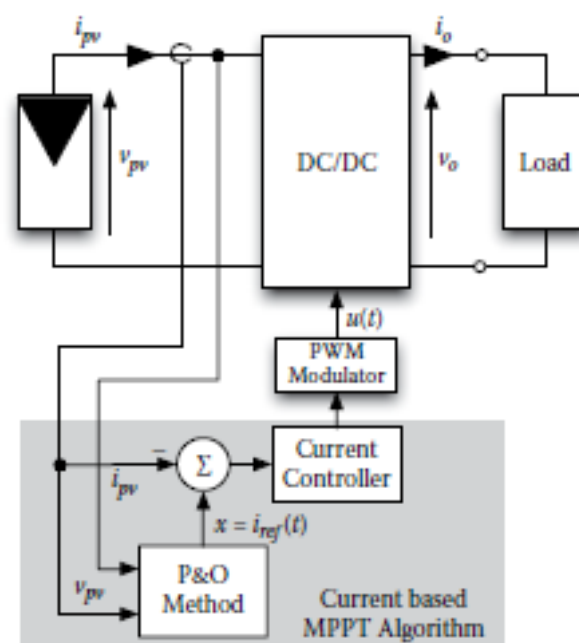
FIGURE 3.13
Control scheme of the current-based MPPT.

other side, the linear dependency of the PV current on the irradiance level would be very useful for a fast current-based MPPT, but the occurrence of irradiance drops might lead to the failure of configurations based on the direct regulation of the PV current. Figure 3.13 shows the basic scheme of a PV current regulator. In terms of MPPT control, it is the dual configuration of Figure 2.6b.
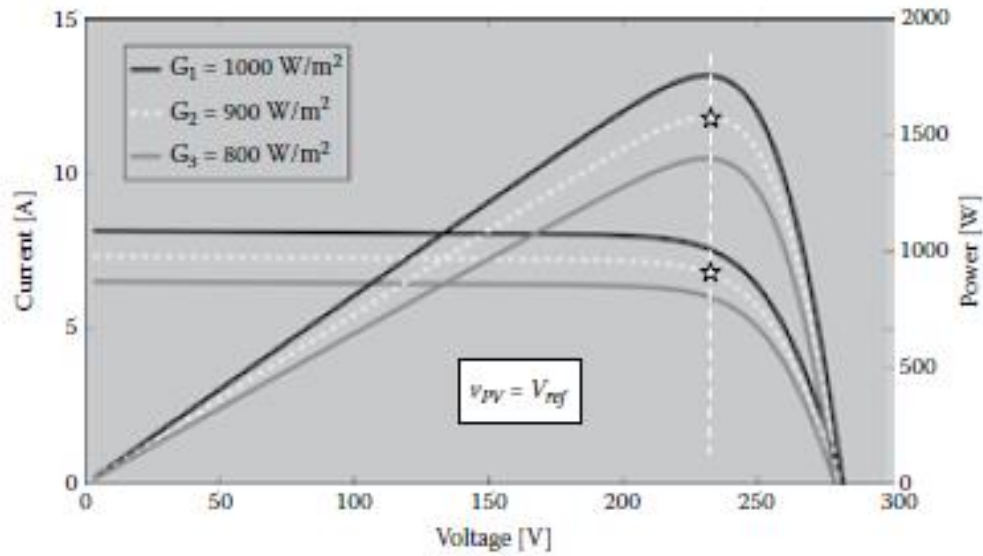
FIGURE 3.14
P-V and I-V curves at different irradiance levels: voltage-based MPPT.

star in Figure 3.14, is fixed at the same irradiance level of the previous case by the current-controlled MPPT technique by imposing $i_{ref} = I_{MPP(G_2)}$. Where $I_{MPP(G_2)}$ corresponds to the current delivered by the PV field when it operates in MPP at the irradiance level G2. At this value of the reference current, in the presence of an irradiance variation, the PV operating point moves vertically. Figure 3.15 shows that an increase of irradiance moves the operating
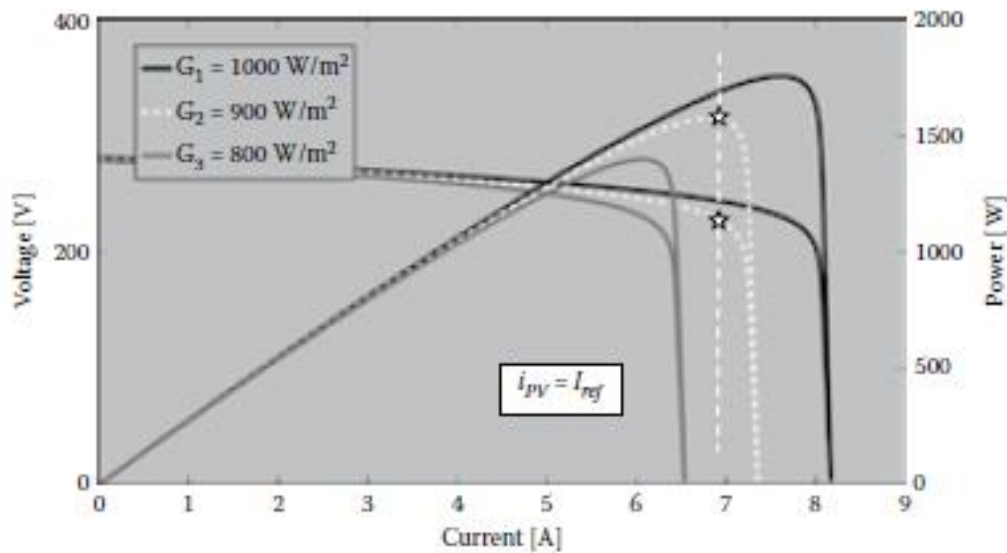

FIGURE 3.15
P-I and V-I curves at different irradiance levels: current-based MPPT.

3.3 Sliding Mode in PV System

In the previous paragraphs it has been shown that in grid-connected PV systems, like the one depicted in Figure 3.16, the inverter operation generates an oscillation of the voltage of the bulk capacitor C_b at a frequency equal to twice the grid frequency, which propagates through the MPPT DC/DC converter and affects the photovoltaic voltage, thus degrading the MPPT efficiency.

In literature, solutions avoiding large DC-link capacitance C_b have been proposed. They are mostly based on complex architectures that penalize the efficiency and reliability [18]. The linear voltage-mode-based controllers used in [2] and in Section 3.1.1 specifically to reject the disturbances coming from the grid in some cases suffer a possibly not easy design of the compensation network to comply with worst-case conditions and limited robustness whenever both continuous conduction mode (CCM) and discontinuous conduction mode (DCM) operating conditions occur, e.g., during irradiance transitions from high to low levels.

This paragraph shows how the low-frequency ripple mitigation can be achieved by means of the sliding mode control (SMC). Such a nonlinear control technique can be very effective in ensuring extreme robustness and fast response, not only in applications involving switching converters [19–21], but also in more complex power electronic systems [22, 23]. SMC is based on the
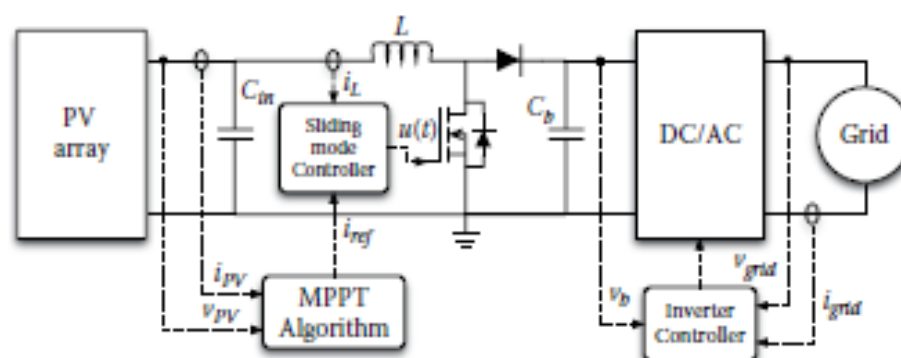

FIGURE 3.16
MPPT P&O with direct perturbation of the reference current.

$$\Psi = i_L - i_{ref} = 0 \qquad\qquad (3.30)$$

where the reference current i_{ref} can be provided by a classical perturbative MPPT controller. Figure 3.17 shows a possible implementation of the SMC with two comparators and a flip-flop. Such a simple scheme can be directly used to generate the signals driving the MOSFET gates:

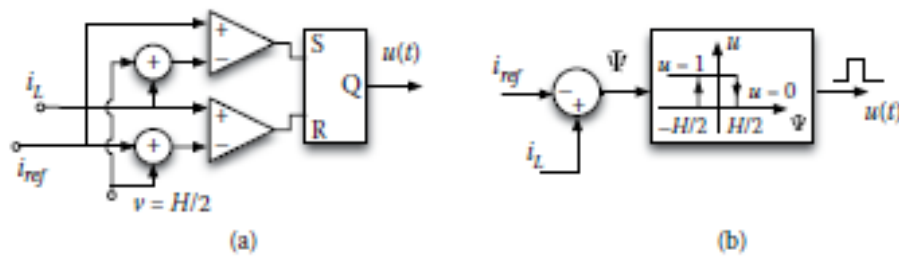$$\begin{cases} i_L < i_{ref} - \dfrac{H(t)}{2} & \text{turn ON MOSFET} \\[2ex] i_L > i_{ref} + \dfrac{H(t)}{2} & \text{turn OFF MOSFET} \end{cases} \qquad (3.31)$$

(a)   (b)

FIGURE 3.17
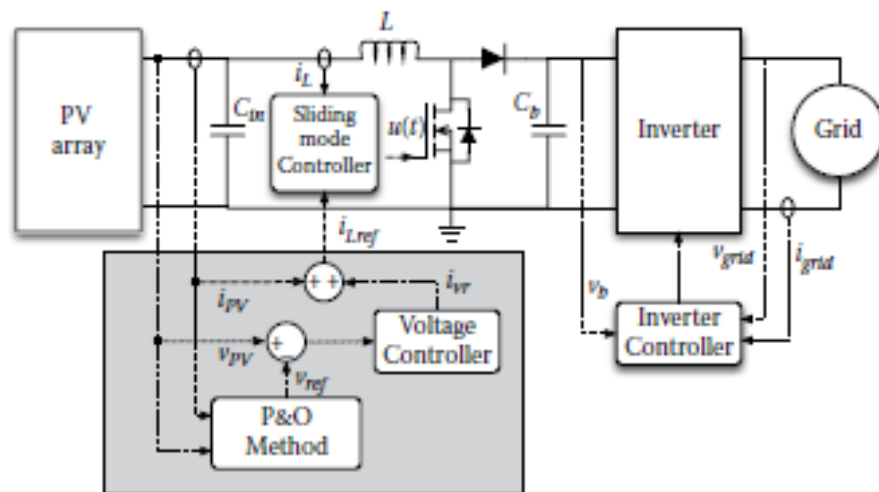Sliding mode controller. (a) Practical implementation. (b) Logic scheme.

FIGURE 3.23
Sliding mode architecture for compensating the fast PV current variation.

Using the previous expression in the sliding control equation, $\Psi = i_{Lref}(t) - i_L(t) = 0$, leads to the following simplification:

$$\Psi = i_{C_{in}} + i_L + i_{zr} - i_L = 0 \tag{3.54}$$
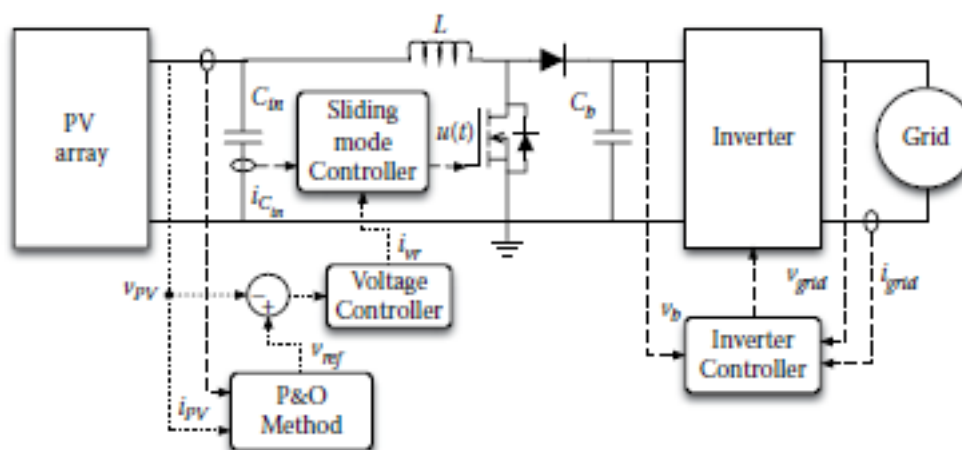
$$\Psi = i_{C_{in}} + i_{zr} = 0 \tag{3.55}$$

FIGURE 3.24
System scheme based on input capacitor current control.

3.4.1 Noise Attenuation by Using Low-Pass Filters

Processing the measured signals by means of a low-pass filter (LPF) is the first method for attenuating the effects of the noise. This method, however, should be applied carefully in order to avoid suppressing useful information, destabilizing the MPPT control loop, or sacrificing its promptness. Indeed,
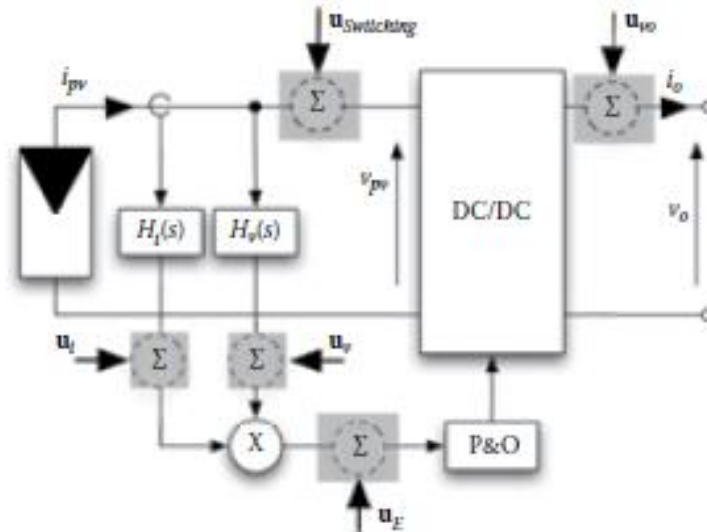

FIGURE 3.31
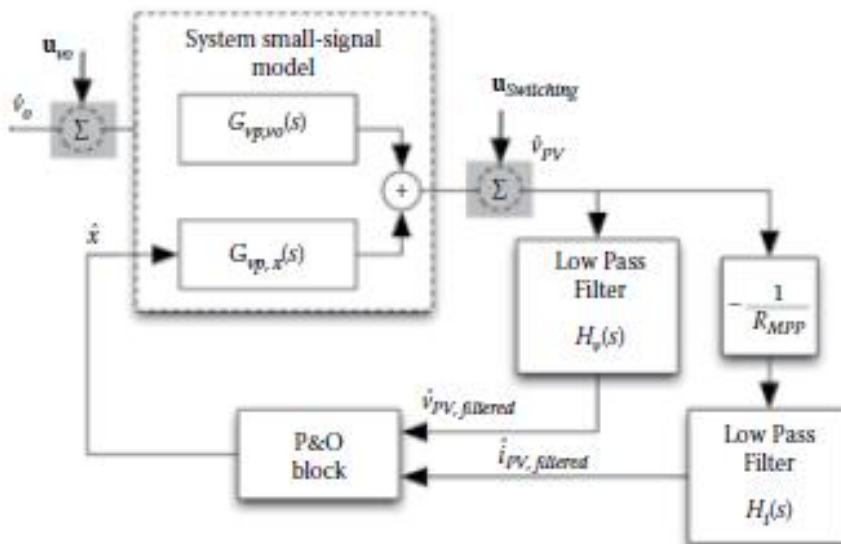Uncertainty distribution in a P&O MPPT switching converter.

FIGURE 3.32
Effect of the LPF on the MPPT dynamics.

Read Page 129 to 138

4

Distributed Maximum Power Point Tracking of Photovoltaic Arrays

4.1 Limitations of Standard MPPT

Photovoltaic (PV) systems usually adopt field maximum power point tracking (FMPPT), that is, the tracking of the maximum power point (MPP) of the power vs. voltage (P-V) characteristic of the whole field composed by paralleled PV strings (Figure 4.1).

In case of mismatch (due to clouds, shadows, dirtiness, manufacturing tolerances, aging, different orientation of parts of the PV field, etc.), the P-V characteristic of the PV field may exhibit more than one peak, due to the adoption of bypass diodes, and MPPT algorithms can fail, causing a severe decrease in the overall system efficiency [1–34], unless the whole P-V characteristic is periodically swept. Even when FMPPT is able to catch the absolute maximum power of the mismatched PV field, such a power is lower than the sum of the available maximum powers that the mismatched modules are able to provide.

4.2 A New Approach: Distributed MPPT

The solution adopted to overcome the drawbacks associated to mismatching phenomena in PV applications is called distributed maximum power point tracking (DMPPT). Two different DMPPT approaches can be used. The first one is based on the adoption of module-dedicated DC/AC converters, called microinverters, and realizing the MPPT for each PV module [35–37]. The second approach is instead based on the use of module-dedicated DC/DC converters, realizing the MPPT for each module and centralized inverters [45–64].
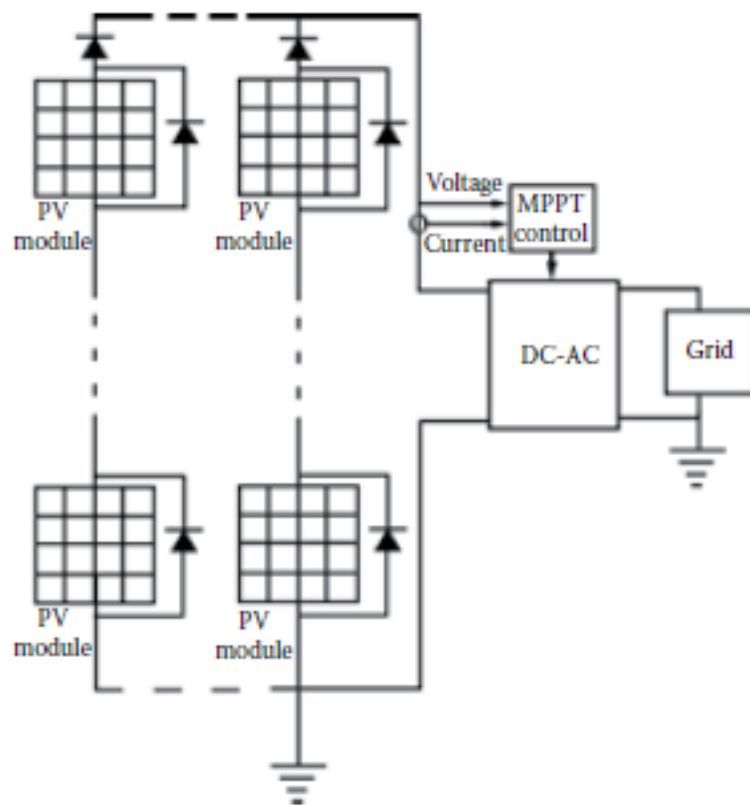
FIGURE 4.1
Grid-connected PV system with FMPPT. Strings of PV modules are put in parallel and connected to a single DC/AC inverter.

4.2.1 DMPPT by Means of Microinverters

A microinverter is a DC/AC grid-connected device that converts the DC power from a single PV module to grid-compliant AC power and carries out the MPPT on such a module (Figure 4.2) [35–37].

The advantages provided by the adoption of microinverters are the following:

- Almost no waste of available PV energy in case of mismatching.
- Modularity, because PV systems can be easily expanded by simply paralleling microinverters at the AC side.
- Each module works independently. If one module fails, the other modules will continue to deliver power to the grid.
- Low minimum system size. That is, the threshold for people to start their own PV plant is lowered.
- Use of standard AC installation material (no DC cabling), which reduces costs of installation material and system design.
- No need for string diodes, and therefore no additional conduction losses due to the presence of blocking diodes.
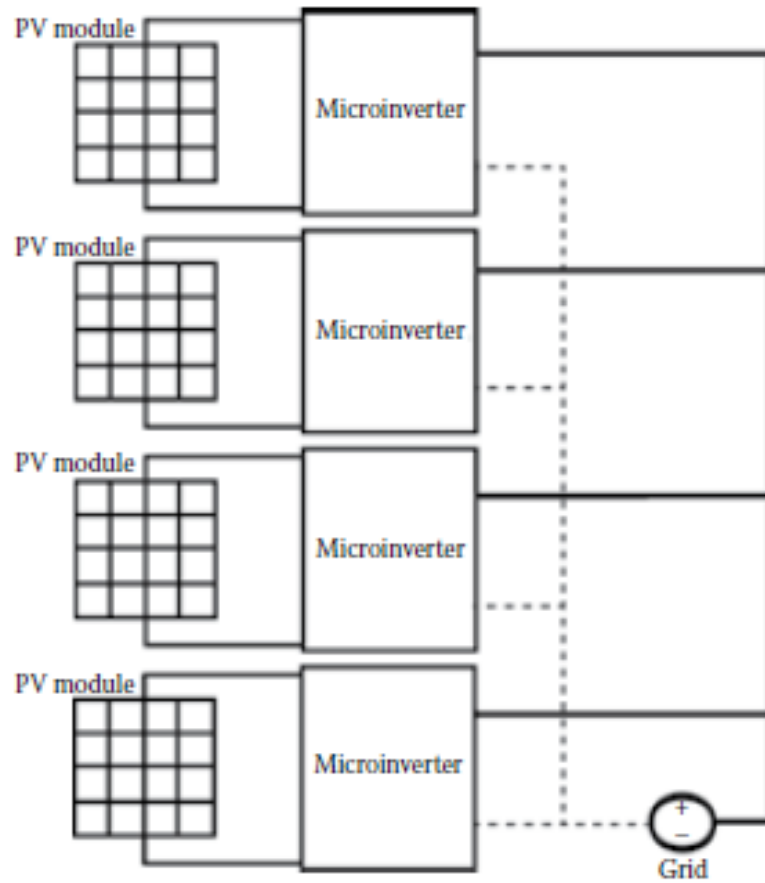
FIGURE 4.2
Grid-connected PV system with DMPPT. Approach based on the adoption of microinverters with the output ports in parallel to the grid.
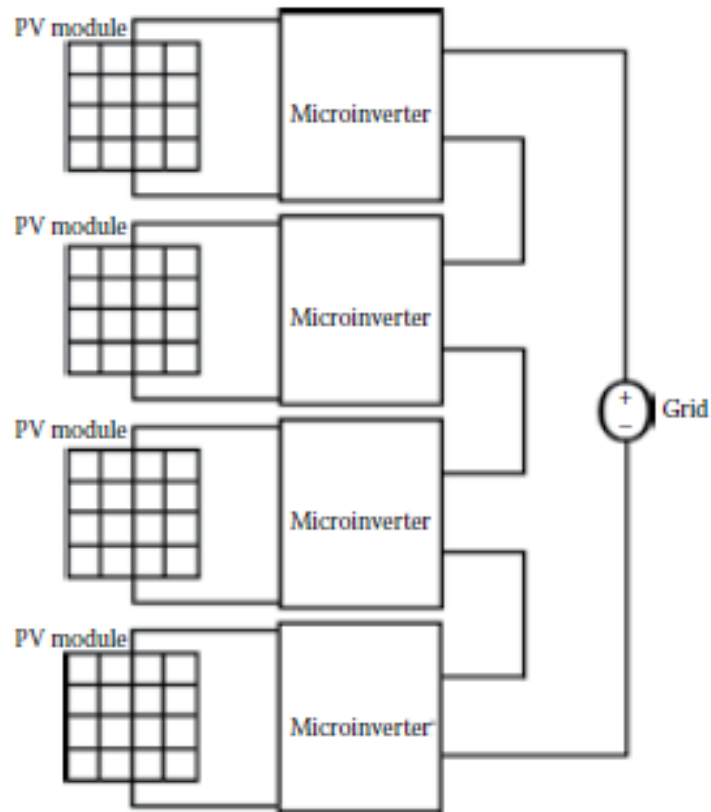
FIGURE 4.3
Grid-connected PV system with DMPPT. Approach based on the adoption of microinverters with the output ports connected in series.
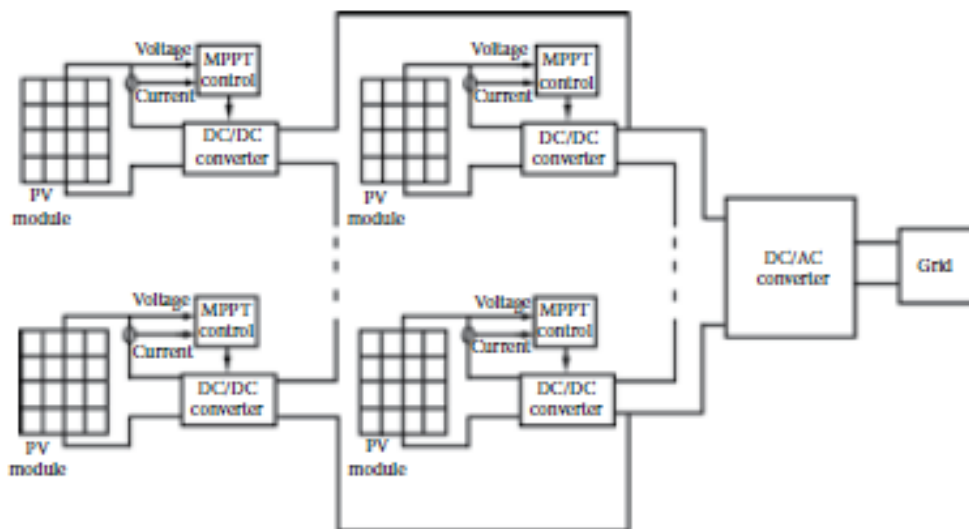

FIGURE 4.4
Grid-connected PV system with DMPPT. Approach based on the adoption of MPPT DC/DC converters with the output ports connected in series.

switching control photovoltaic modules SVPVM

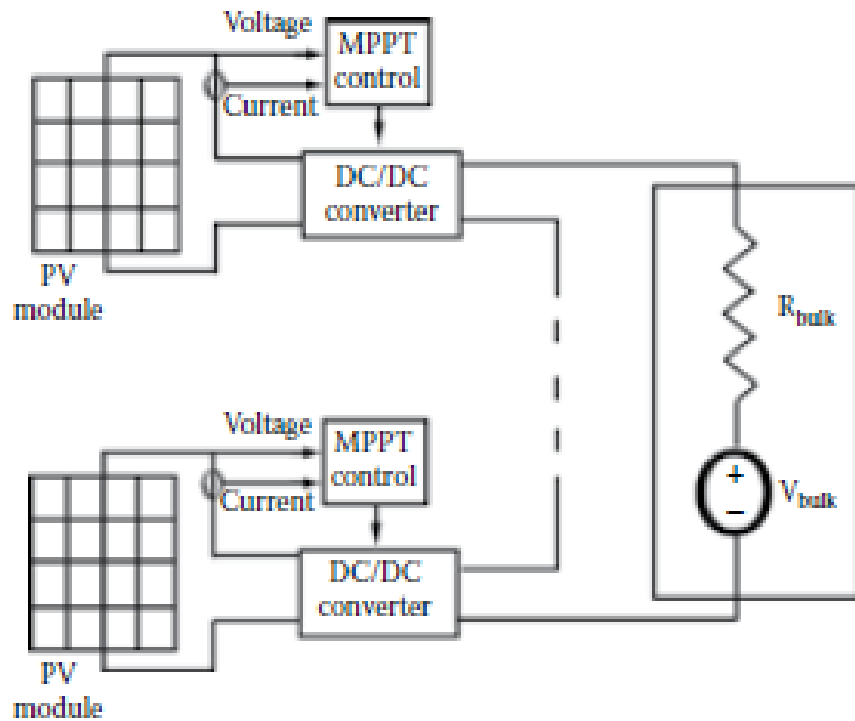Read Page 152 to 200—Characteristics data

FIGURE 4.106
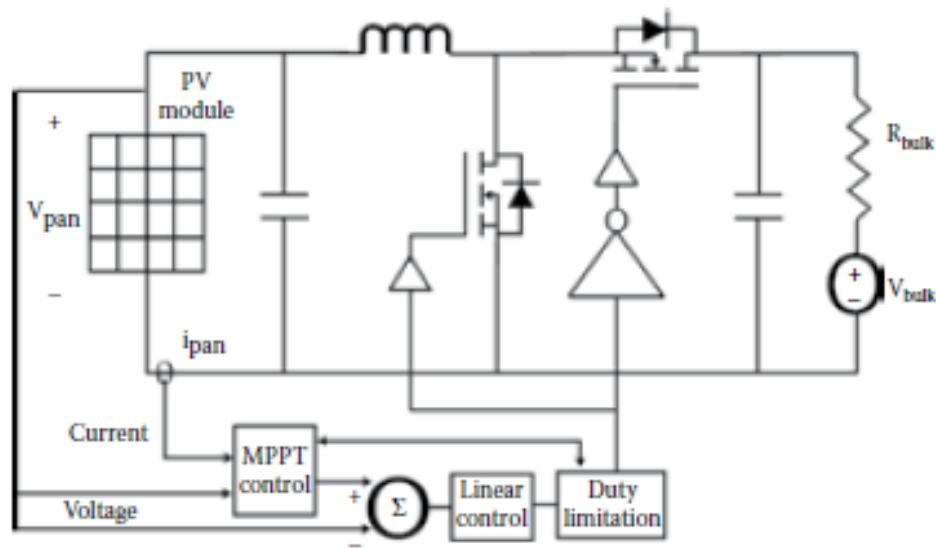Simplified model of a string of SCPVMs.

FIGURE 4.107
Schematic of an SCPVM employing a boost converter with synchronous rectification, input voltage feedback control, and dynamic duty cycle limitation.

like V, I, and D are used to indicate DC values of the same variables; and small letters with hat symbols indicate small-signal variations around their steady-state operating point.

4.5.1.1 Open-Loop Transfer Functions of an SCPVM

The following transfer functions can be defined and computed by analyzing the circuit of Figure 4.110:

$$G_{vpan\ d\ OL}(s) = \left. \frac{\hat{v}_{pan}(s)}{\hat{d}(s)} \right|_{\substack{\hat{i}_g(s)=0 \\ \hat{v}_{bulk}(s)=0 \\ \text{open loop}}} \tag{4.4}$$

$$G_{ibulk\ d\ OL}(s) = \left. \frac{\hat{i}_{bulk}(s)}{\hat{d}(s)} \right|_{\substack{\hat{i}_g(s)=0 \\ \hat{v}_{bulk}(s)=0 \\ \text{open loop}}} \tag{4.5}$$

$$Z_{vpan\ i_g\ OL}(s) = \left. \frac{\hat{v}_{pan}(s)}{\hat{i}_g(s)} \right|_{\substack{\hat{d}(s)=0 \\ \hat{v}_{bulk}(s)=0 \\ \text{open loop}}} \tag{4.6}$$
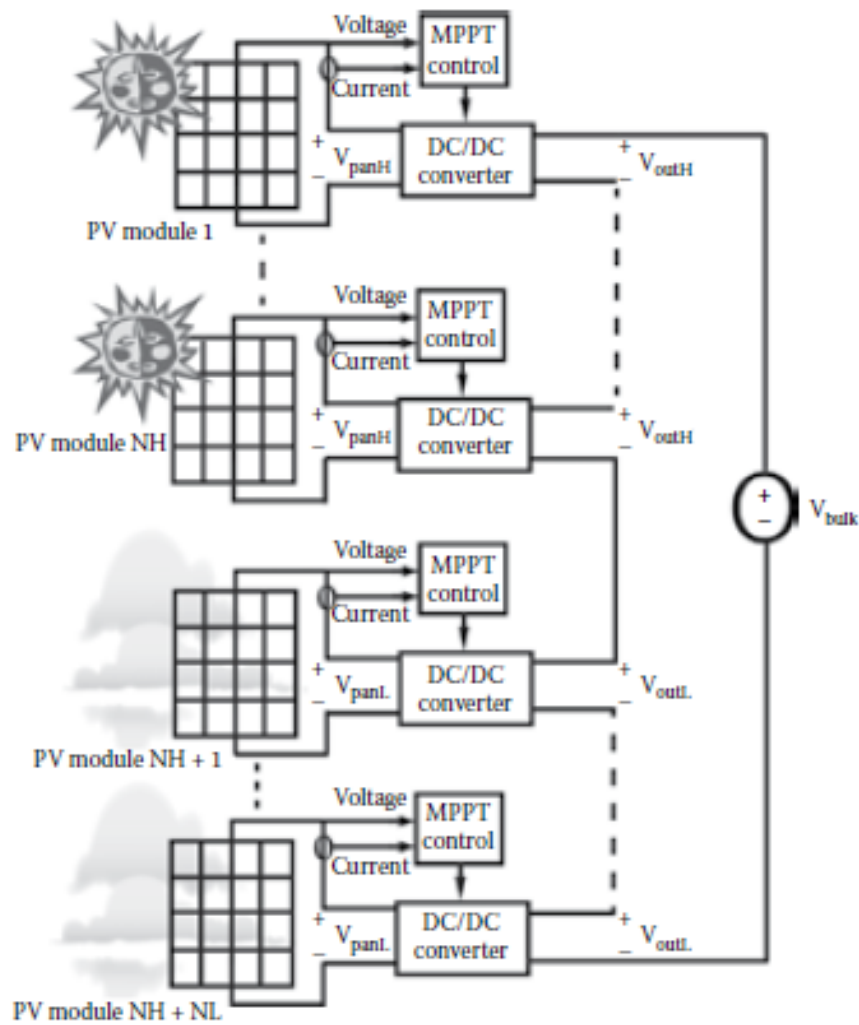
FIGURE 4.108
Simplified model of a string of SCPVMs under uneven irradiation.
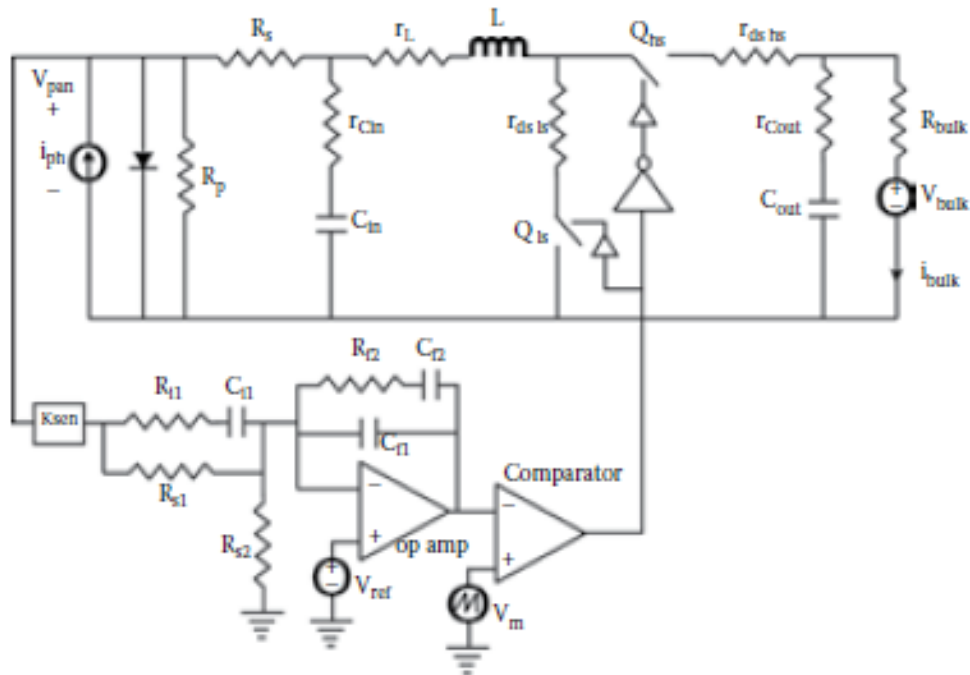
FIGURE 4.109
Schematics of an SCPVM under study (i_{ph}, Rp, and Rs are the parameters of the large-signal model of the PV module; see Chapter 1).

$$Z_{out\ OL}(s) = -\left.\frac{\hat{v}_{bulk}(s)}{\hat{i}_{bulk}(s)}\right|_{\substack{\hat{i}_g(s)=0 \\ \hat{d}(s)=0 \\ open\ loop}} \tag{4.9}$$

Input voltage control is implemented via a standard operational amplifier with negative feedback. Its dynamics is described by the transfer function

$$G_c(s) = \frac{Z_f(s)}{Z_i(s)} \tag{4.10}$$

where

$$Z_f(s) = (R_{f2} + \frac{1}{sC_{f2}})||\frac{1}{sC_{f1}} \tag{4.11}$$

$$Z_i(s) = (R_{i1} + \frac{1}{sC_{i1}})||R_{s1} \tag{4.12}$$

FIGURE 4.110
Small-signal model of the SCPVM.

FIGURE 4.111
Block diagram of the small-signal AC model of the SCPVM of Figure 4.110.
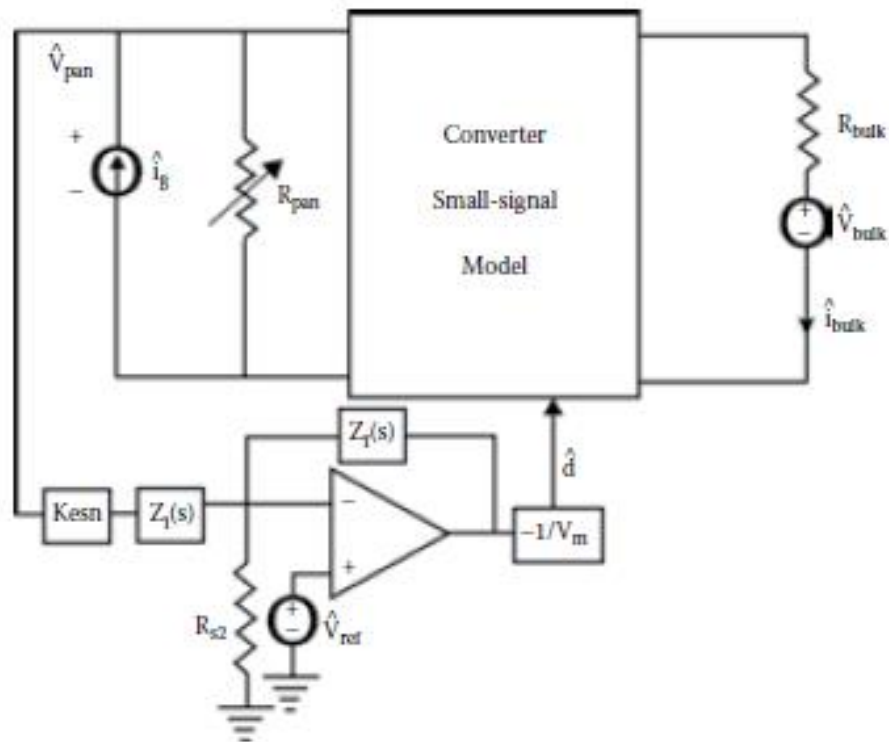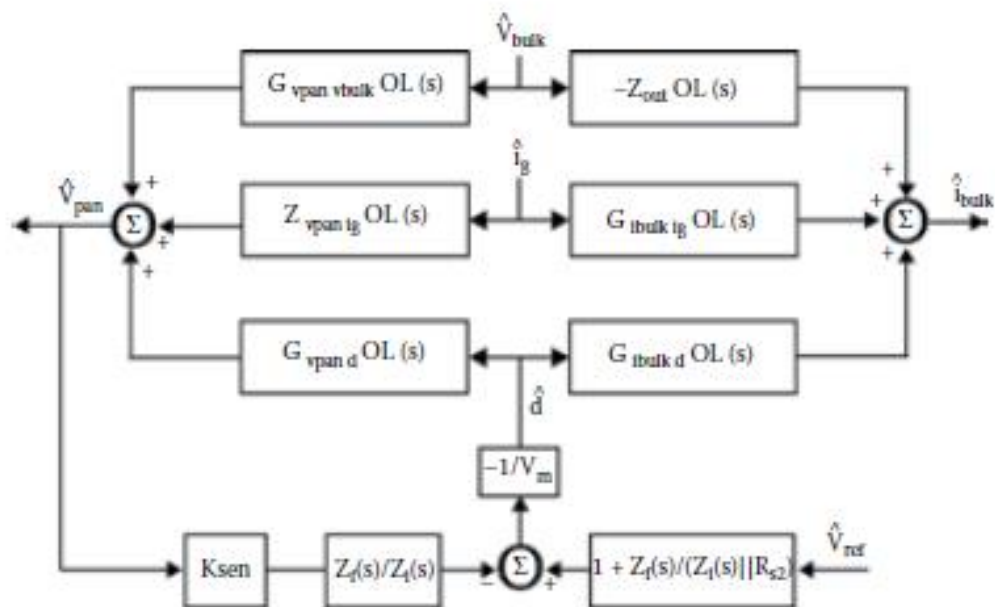
4.5.1.2 Closed-Loop Transfer Functions of an SCPVM

The block diagram of Figure 4.111 schematizes the dynamic interactions between input and output variables of the SCPVM of Figure 4.110 and allows the computation of the closed-loop input-to-output transfer functions of the SCPVM.

$$G_{v_{pan}v_{ref}CL}(s) = \frac{\hat{v}_{pan}(s)}{\hat{v}_{ref}(s)}\Bigg|_{\substack{i_g(s)=0 \\ \hat{v}_{bulk}(s)=0 \\ \text{closed loop}}} = \frac{\left[1 + \dfrac{Z_f(s)}{Z_i(s)R_{s2}}\right]G_{v_{pan}\,dOL}(s)\dfrac{1}{V_m}}{1 + T_c(s)} \qquad (4.14)$$

$$G_{i_{bulk}\,v_{ref}CL}(s) = \frac{\hat{i}_{bulk}(s)}{\hat{v}_{ref}(s)}\Bigg|_{\substack{i_g(s)=0 \\ \hat{v}_{bulk}(s)=0 \\ \text{closed loop}}} = \frac{\left[1 + \dfrac{Z_f(s)}{Z_i(s)R_{s2}}\right]G_{i_{bulk}\,dOL}(s)\dfrac{1}{V_m}}{1 + T_c(s)} \qquad (4.15)$$

$$G_{v_{pan}\,v_{bulk}CL}(s) = \frac{\hat{v}_{pan}(s)}{\hat{v}_{bulk}(s)}\Bigg|_{\substack{i_g(s)=0 \\ v_{ref}(s)=0 \\ \text{closed loop}}} = \frac{G_{v_{pan}\,v_{bulk}OL}(s)}{1 + T_c(s)} \qquad (4.16)$$

$$Z_{out\,CL}(s) = -\frac{\hat{v}_{bulk}(s)}{\hat{i}_{bulk}(s)}\Bigg|_{\substack{i_g(s)=0 \\ v_{ref}(s)=0 \\ \text{closed loop}}} = \frac{Z_{out\,OL}(s)}{1 - \dfrac{Z_{out\,OL}(s)\,G_{i_{bulk}\,d\,OL}(s)G_{v_{pan}v_{bulk}\,OL}(s)K_{sen}G_c(s)\dfrac{1}{V_m}}{1 + T_c(s)}}$$

$$(4.17)$$
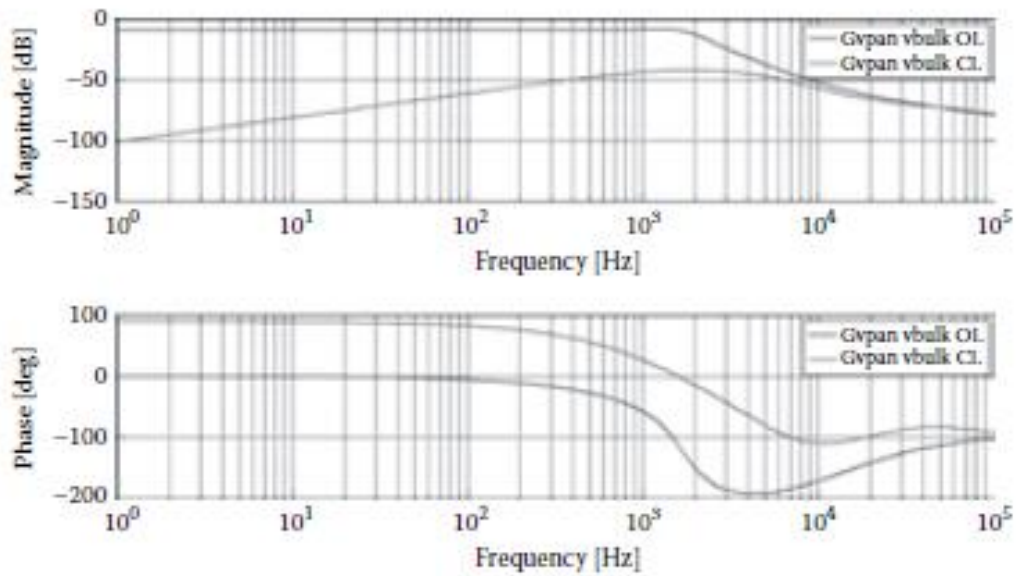
FIGURE 4.112
Output voltage to input voltage transfer function of the circuit of Figure 4.109 in open-loop (OL) and closed-loop (CL) conditions.

$$G_{i_{bulk}\ i_g\ CL}(s) = \left.\frac{\hat{i}_{bulk}(s)}{\hat{i}_g(s)}\right|_{\substack{\hat{v}_{bulk}(s)=0 \\ \hat{v}_{ref}(s)=0 \\ closed\ loop}} = G_{i_{bulk}\ i_g\ CL}(s) + \frac{G_{i_{bulk}\ d\ OL}(s)Z_{v_{bulk}\ i_g\ OL}(s)K_{sen}G_c(s)\frac{1}{V_m}}{1+T_c(s)}$$

(4.18)

$$Z_{v_{pan}\ i_g\ CL}(s) = \left.\frac{\hat{v}_{pan}(s)}{\hat{i}_g(s)}\right|_{\substack{\hat{v}_{bulk}(s)=0 \\ \hat{v}_{ref}(s)=0 \\ closed\ loop}} = \frac{Z_{v_{pan}\ i_g\ OL}(s)}{1+T_c(s)}$$

(4.19)

Read Page 201 to 244 about various technical facts
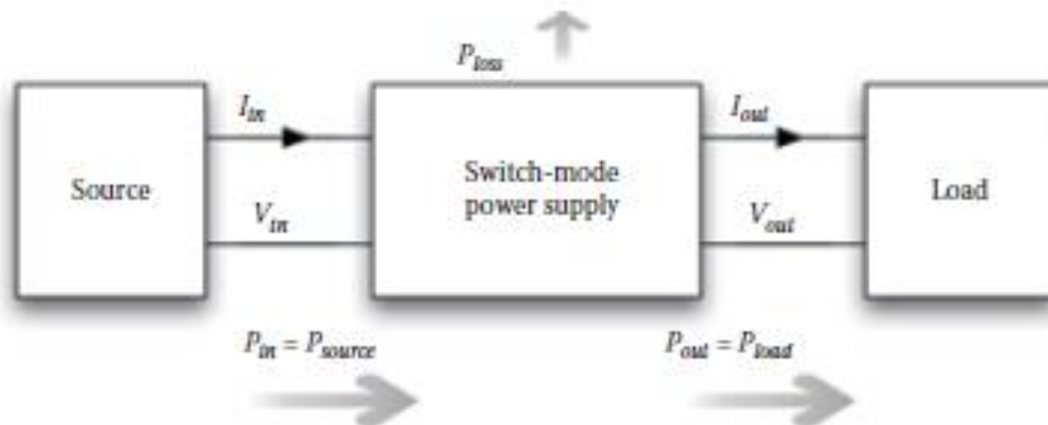
SMPS- switching Mode Power Supply

FIGURE 5.1
SMPS intput, output and loss power.

The SMPS power losses P_{loss} depend on many influence factors, like the input and output ports' *termination conditions* (V_{in}, I_{in}, V_{out}, I_{out}), the *switching frequency* (f_s), the *physical parameters* of the devices where the losses take place (p), and the *ambient temperature* (T_a). The exact dependence of P_{loss} on the influence factors is quite involved. The achievement of an SMPS design complying with given efficiency requirements is possible only if adequate loss models are used. Efficiency requirements greatly depend on the application. If both source and load are time invariant, the analysis of efficiency is limited to a fixed set of port termination conditions. This is the simplest case, as the efficiency reduces to a function—though involved—of switching frequency and temperature. Unfortunately, most applications involve some variation of load, source, or both. Consequently, the efficiency also has to be analyzed with respect
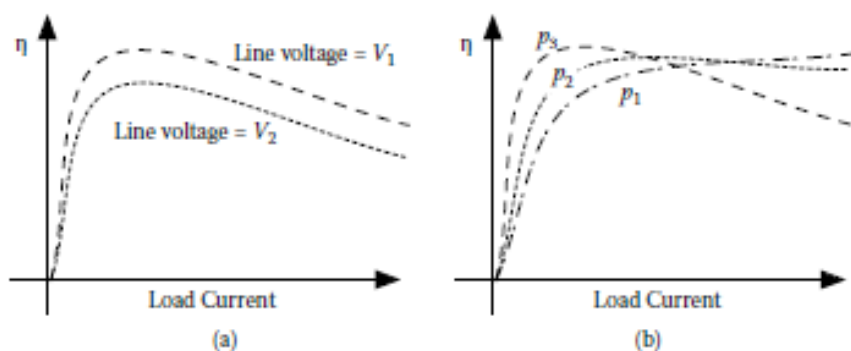
FIGURE 5.2
Efficiency curves of a switch-mode power supply. (a) Fixed parameters, different line voltage values. (b) Fixed line voltage, different FET parameter values.

to the termination conditions to identify the worst case. Typical plots of SMPS power efficiency with respect to load current and line voltage variations are shown in Figure 5.2. The plots show two fundamental elements characterizing the efficiency.

$$\eta_P = \frac{UI_{load}}{UI_{source}} = \frac{U_{out}}{U_{in}} = \frac{\displaystyle\int_{t_s}^{t_e} v_{out}(t)i_{out}(t)dt}{\displaystyle\int_{t_s}^{t_e} v_{in}(t)i_{in}(t)dt}$$

(a)

(b)

FIGURE 5.3
(a) PV-MPPT SMPS. (b) Point-of-load SMPS.

$$\text{PV: } U_{in} = \int_{t_s}^{t_e} v_{in}(t)i_{in}(t)dt \quad U_{out} = \int_{t_s}^{t_e} v_{in}(t)i_{in}(t)\eta(\underline{tc}, \underline{p}, f_s, T_a)dt \qquad (5.5)$$

$$\text{POL: } U_{in} = \int_{t_s}^{t_e} \frac{v_{out}(t)i_{out}(t)}{\eta(\underline{tc}, \underline{p}, f_s, T_a)}dt \quad U_{out} = \int_{t_s}^{t_e} v_{out}(t)i_{out}(t)dt \qquad (5.6)$$

5.3 Energy Harvesting in PV Plant Using DMPPT Power Converters

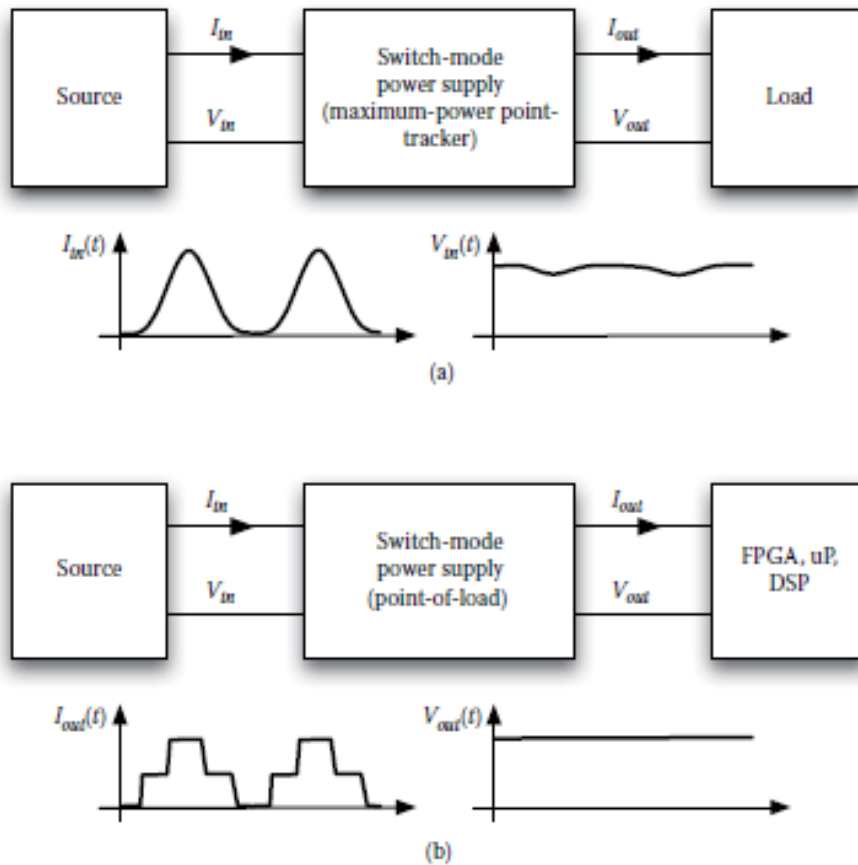Let us consider the case discussed in Chapter 4, where the PV source is made of a couple of Sunmodule SW225 PV panels (V_{oc} = 36.8 V, I_{sc} = 8.17 A, V_{MPP} = 29.5 V, I_{MPP} = 7.63 A, $NOCT$ = 46°C), each one equipped with a DMPPT DC/DC power converter of boost or buckboost topology. In Chapter 4 the analysis of the mismatched operation was done with reference to a generic condition characterized by sun irradiances of 1000 W/m² for one panel and 500 W/m² for the other one. Here we consider in more detail a realistic condition referred to real daily sun irradiance and temperature data and to the presence of a body shading the two panels in nonuniform way. Plots of Figure 5.4 show the daily evolution of sun irradiance and ambient temperature recorded on September 15, 2001, in Napoli, Italy (40° 50′ 23.940″ N, 14° 15′ 9.152″ E). During that day, the sun irradiance reached a quite high peak value, near 1200 W/m², due to a very clean sky. The temperature held mostly in the range from 20°C to 23°C. The day was close to autumn equinox, so that there were almost 12 light hours. Table 5.2 summarizes the azimuth and incidence angles of sun irradiance with respect to the PV panel surface.

The panels are assumed to be installed over a flat surface, oriented south and tilted 40°, equal to the city of Napoli latitude. Right side plots of Figure 5.4 show the corresponding path of MPP of one unshaded 225 W PV panel in the I vs. V and P vs. V planes, with a 10 min sampling time interval.
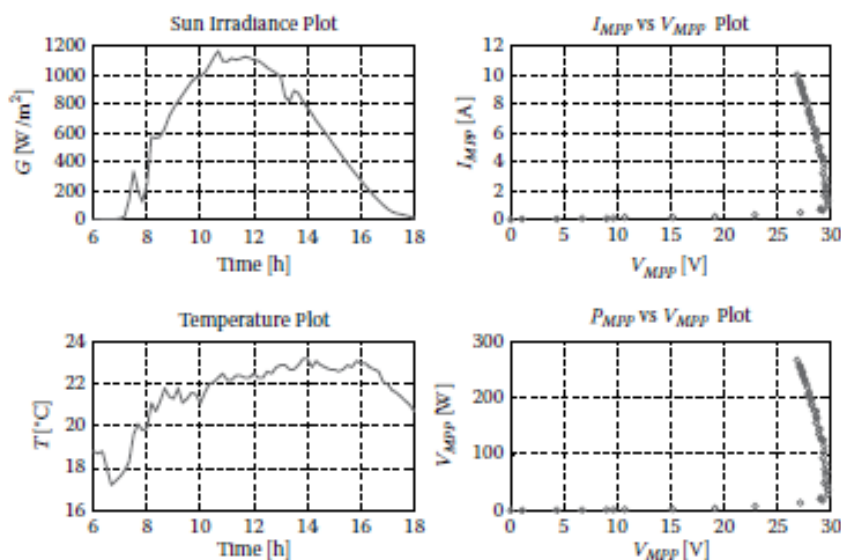

FIGURE 5.4
Sun irradiance, temperature data, and related MPP voltage, current, and power data of 225 Wp PV panel.

5.4 Losses in Power Converters

The selection of power devices and switching frequency allowing a reliable achievement of the application efficiency targets can be achieved only through the analysis of the efficiency as a function of the SMPS topology, operation mode, termination conditions, switching frequency, thermal conditions, and power device parameters. This is possible only if adequate loss models at device level and circuit level are adopted. The models must be sufficiently detailed and accurate to provide reliable results; however, they cannot be too detailed because some elements influencing the power losses, like stray inductances of Printed Circuit Board (PCB) traces, are not known until the SMPS design is complete, including power devices and housekeeping circuitry, and the PCB routing is done. A second important issue is related to how the parameters of power devices used in the loss models are extracted from datasheets, where some numerical data are provided for certain reference operating conditions and more complete data are available in graphic format. Using different combinations of loss model approximations and parameter approximations can lead to much different power loss predictions: This may have a big impact on power device selection and the achievement of energy efficiency design goals.

The silicon and magnetic devices are responsible for the majority of power losses of SMPS. The loss mechanisms of these devices are not easy to model, as they are connected to various nonlinear physical phenomena and are heavily conditioned by frequency and temperature. For silicon devices, switching losses are much more difficult to calculate than conduction losses. They are influenced by many factors:

- *Converter topology*: Different topologies involve different voltage/current stresses.
- *Operation mode*: SMPS may operate as hard switching, soft switching, resonant, etc.
- *Load/line range*: Some applications require operation over wide line/load ranges, which involve wide changes of device stress and related losses and possible lack of soft switching.
- *Device technology*: Materials, physical structures, operation principles, and parameter sensitivity of devices are much diversified, and thus so are their loss mechanisms.
- *Drivers*: Switching times depend on drive maximum current and adaptive dead time management capabilities.

factors influencing magnetic device losses in SMPS are:

- *Converter topology, mode of operation, line/load ranges*: These factors determine the voltage and current stresses.
- *Core material*: The power loss density and its dependence on frequency and temperature change very much depending on which ferrite or powdered iron core is used.
- *Windings*: Windings losses can dramatically increase due to skin and proximity effects.

Intradevice heat flows and transfers: Heat flows in a quite complicated way through the core and also passes from the core to the windings or vice versa, depending on which part is hotter.

Lack of thermal coefficients: The physical structure of most inductors and transformers makes it very difficult to determine intradevice and device-to-air convection coefficients needed to model the heat transfer; most device manufacturers do not provide any thermal data.

Nonlinearity: The complete magneto-electro-thermal model of a magnetic device is quite puzzling, due to heavy nonlinearity involving interdependence among physical and geometrical parameters.

5.5 Losses in the Synchronous FET Switching Cells

A wide variety of topologies and switching techniques are adopted for power converter design and realization. Nevertheless, the loss mechanisms in switching devices can be described by referring to the basic configuration made of a couple of synchronous FETs shown in Figure 5.11a. The switching cell of Figure 5.11a is the brick of most PWM hard-switching inductive power converters, like the boost and buckboost of Figure 5.11b and 5.11c.

The following discussion will be focused on this specific and elementary case, as the goal is to illustrate in depth a loss-controlled design methodology for high-efficiency applications, aimed at supporting a systematic and reliable real power components selection using the parameter values available in component datasheets and application notes. Similarly, other elementary cells for soft-switching converters, as well as for switched capacitor converters, could be identified, providing the fundamentals for the derivation of pertinent loss models that can be used with the same design approach.

The switching cell of Figure 5.11, in manifold variants, has been widely discussed and modeled in literature to describe the behavior of switching converters for both loss analysis and static and dynamic behavioral analysis. In the present discussion, the cell will be used to highlight the basic voltage/current stress correlations, which provide the reference operating parameters for loss calculations and device selection. The two switches operate under the action of a driver controller, ensuring that when a FET is ON, the
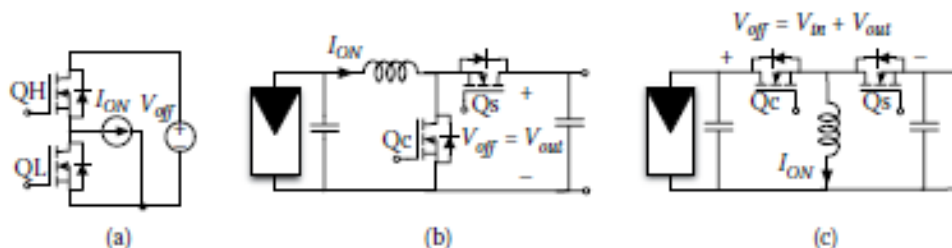

FIGURE 5.11
(a) Synchronous switching cell. (b) Boost topology. (c) Buckboost topology.
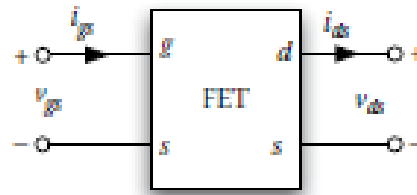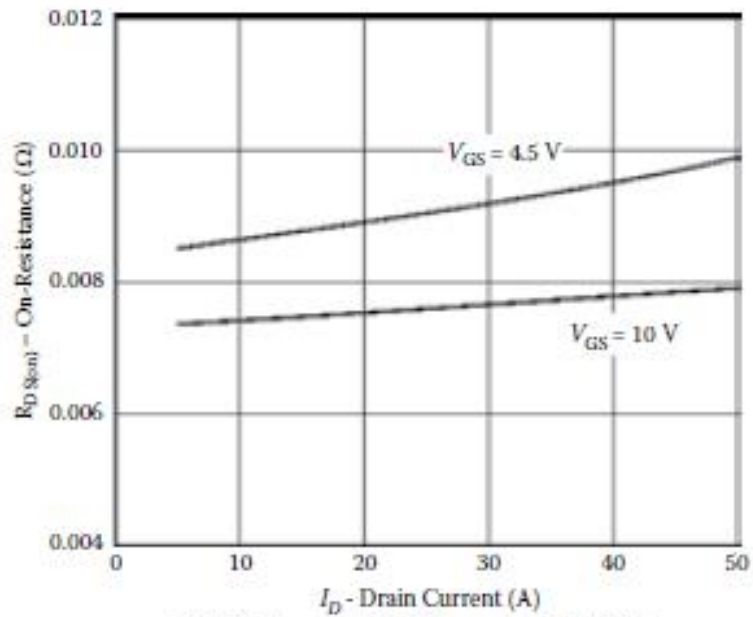
FIGURE 5.12
Two-port model of a MOSFET.

$$P_d = f_s \int_0^{T_s} \left[v_{gs}(t)i_{gs}(t) + v_{ds}(t)i_{ds}(t) \right] dt = P_c + P_{sw,on} + P_{sw,off}$$

$$= f_s \left[\int_{T_c} v_{ds}(t)i_{ds}(t)dt + \sum_{i=1}^{N_{on}} \int_{T_{on,i}} \left(v_{gs}(t)i_{gs}(t) + v_{ds}(t)i_{ds}(t) \right) dt + \sum_{j=1}^{N_{off}} \int_{T_{off,j}} \left(v_{gs}(t)i_{gs}(t) + v_{ds}(t)i_{ds}(t) \right) dt \right]$$

5.6 Conduction Losses

The first integral term in square brackets in Equation (5.7) provides the *conduction losses*. The integral argument of this term is limited to the power product $v_{ds}(t)i_{ds}(t)$ as $i_{gs}(t) = 0$ during the ON state conduction subinterval T_C. If $v_{gs}(t)$ is sufficiently high, the FET will be operating in the ohmic region, and the voltage $v_{ds}(t)$ can be approximately expressed as $v_{ds}(t) = R_{ds,on}i_{ds}(t)$, where $R_{ds,on}$ is the FET channel resistance. For some devices, if $v_{gs}(t)$ is sufficiently high and if the magnitude swing of current $i_o(t)$ during the subinterval T_c is sufficiently limited, then $R_{ds,on}$ can be considered constant and then conduction losses are expressed by the simplified Equation (5.8):

$$P_c = f_s \int_{t_{c1}}^{t_{c2}} v_{ds}(t)i_{ds}(t)dt = R_{ds,on} f_s \int_{t_{c1}}^{t_{c2}} i_{ds}^2(t)dt = R_{ds,on}I_{ds,rms}^2 \tag{5.8}$$

On-Resistance vs. Drain Current and Gate Voltage

(a)
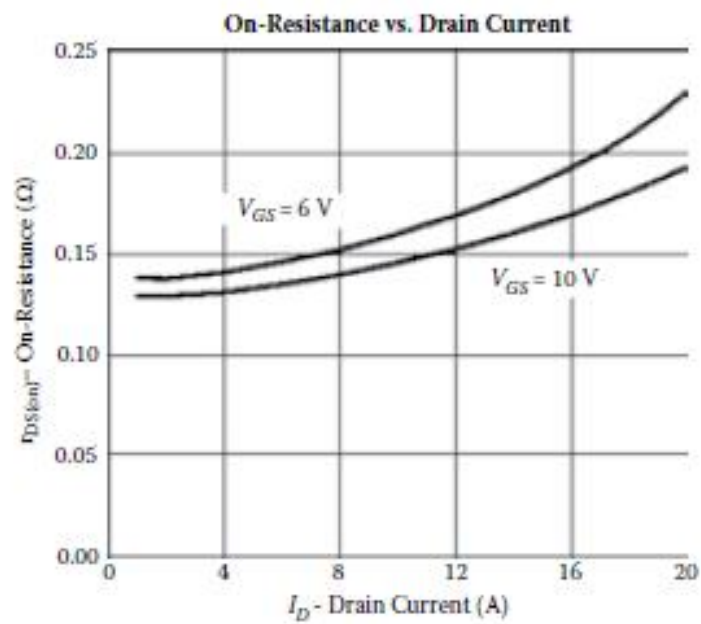
(b)

FIGURE 5.13
Dependency of channel resistance with respect to drain current. (a) Si4840BDY. (b) Si4982DY.
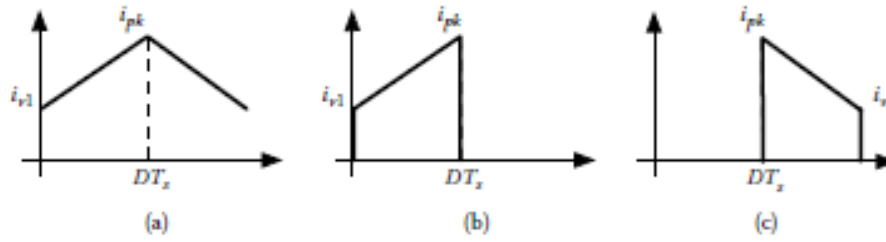(c) Si4892DY.

FIGURE 5.14
(a) $i_o(t)$. (b) $i_{Qc}(t)$. (c) $i_{Qs}(t)$.

cell of Figure 5.11a is working in a hard-switching PWM DC/DC converter, $I_{on}(t)$ looks like the typical triangular waveform of Figure 5.14a (e.g., inductor current in DC/DC converters), and the control and synchronous switch currents, $i_{Qc}(t)$ and $i_{Qs}(t)$, respectively, look like the waveforms of Figure 5.14b and Figure 5.14c, respectively.

Assuming $i_{Qc}(t) = i_{vl} + \alpha t$ (Figure 5.14b), where $\alpha = \Delta i_{opp}/t_{on}$, yields

$$P_c = f_s \int_{i_{cs}}^{i_{ce}} \left[\sum_{k=0}^{N} a_k (i_{vl} + \alpha t)^{k+2} \right] dt = f_s \left[\sum_{k=0}^{N} \frac{a_k \left((i_{vl} + \alpha t_{ce})^{k+3} - (i_{vl} + \alpha t_{cs})^{k+3} \right)}{(k+3)\alpha} \right] \quad (5.10)$$

A simplified form of Equation (5.10) can be obtained by using the average value of $R_{ds,on}$:

$$< R_{ds,on} > = \frac{1}{i_{opp}} \int_{i_{ds,min}}^{i_{ds,max}} R_{ds,on}(i_{ds}) di_{ds} = \frac{1}{i_{opp}} \int_{i_{ds,min}}^{i_{ds,max}} \left[\sum_{k=0}^{N} a_k i_{ds}^k \right] di_{ds}$$

$$= \frac{1}{i_{opp}} \left[\sum_{k=0}^{N} \frac{a_k}{k+1} \left(i_{pk}^{k+1} - i_{vl}^{k+1} \right) \right] \quad (5.11)$$

According to (5.11), an estimation of conduction losses is given by (5.12):

$$P_c = < R_{ds,on} > I_{ds,rms}^2 = \begin{cases} < R_{ds,onQc} > DI_{on} \left[1 + \frac{1}{12} \left(\frac{I_{on,pp}}{I_{on}} \right)^2 \right] & Q_c \\ < R_{ds,onQs} > (1-D)I_{on} \left[1 + \frac{1}{12} \left(\frac{I_{on,pp}}{I_{on}} \right)^2 \right] & Q_s \end{cases} = K_c(\underline{t c}, \underline{p}, f_s, T_a)$$

$$(5.12)$$

which is sufficiently accurate for practical purposes. $\Delta I_{on,pp}$ represents the peak-to-peak ripple magnitude of the source current, whose average value is I_{on}. This current indeed represents the inductor current in DC/DC converters of Figure 5.14.

5.7 Switching Losses

Calculation is much more complicated for switching losses than for conduction losses. The reason is that the waveforms of voltages and currents $v_{ds}(t)$, $i_{ds}(t)$, $v_{gs}(t)$, and $i_{gs}(t)$ during the commutations must be determined taking into account the FET physical parameters influencing the transition from the interdiction region to the linear region passing through the saturation region. A detailed loss analysis is allowed by the knowledge of complete equations describing:

- The nonlinear dependence of the FET channel current on gate-to-source and drain-to-source voltages
- The nonlinear/parametric dependence of FET inter-electrode capacitances on drain-to-source voltage
- The nonlinear dependence of FET body diode current on drain-to-source voltage

Capacitances are fundamental FET parameters for switching loss calculation. The three physical capacitances C_{gs}, C_{gd}, and C_{ds} depend nonlinearly on the absolute value of the drain-to-source voltage $|V_{ds}|$. Their values can be reconstructed from the values of the inter-electrode input capacitance $C_{iss} = C_{gs} + C_{gd}$, reverse capacitance $C_{rss} = C_{gd}$, and output capacitance $C_{oss} = C_{ds} + C_{gd}$. The FET manufacturers provide the curves of the capacitances C_{iss}, C_{rss}, and C_{oss} as functions of $|V_{ds}|$. An example is shown in Figure 5.15, for the same FETs of Figure 5.13.

The three capacitances C_{gs}, C_{gd}, and C_{ds} will be subjected to currents whenever the terminal voltages V_{gs}, V_{gd}, and V_{ds} are subjected to changes. The main difference consists in the fact that C_{gs} and C_{gd} have to be considered as parametric linear capacitances, as their value does not depend directly on their own terminal voltages V_{gs} and V_{gd}, while C_{ds} has to be considered as nonlinear, as its value depends on its own terminal voltage V_{ds}. Accordingly, we have:

$$i_{C_{gs}} = \frac{dQ_{gs}}{dt} = v_{gs}\frac{dC_{gs}(|v_{ds}|)}{d|v_{ds}|}\frac{d|v_{ds}|}{dt}\operatorname{sign}(V_{ds}) + C_{gs}(|v_{ds}|)\frac{dv_{gs}}{dt} \qquad (5.13)$$

$$i_{C_{gd}} = \frac{dQ_{gd}}{dt} = v_{gd}\frac{dC_{gd}(|v_{ds}|)}{d|v_{ds}|}\frac{d|v_{ds}|}{dt}\operatorname{sign}(V_{ds}) + C_{gd}(|v_{ds}|)\frac{dv_{gd}}{dt} \qquad (5.14)$$

$$i_{C_{ds}} = \frac{dQ_{ds}}{dt} = C_{ds}(|V_{ds}|)\frac{dv_{ds}}{dt} \qquad (5.15)$$

Read Page 276 to 290

Page 290 to 308 Design Example